

doi:10.14379/iodp.proc.357.103.2017

Eastern sites¹



G.L. Früh-Green, B.N. Orcutt, S.L. Green, C. Cotterill, S. Morgan, N. Akizawa, G. Bayrakci, J.-H. Behrmann, C. Boschi, W.J. Brazelton, M. Cannat, K.G. Dunkel, J. Escartin, M. Harris, E. Herrero-Bervera, K. Hesse, B.E. John, S.Q. Lang, M.D. Lilley, H.-Q. Liu, L.E. Mayhew, A.M. McCaig, B. Menez, Y. Morono, M. Quéméneur, S. Rouméjon, A. Sandaruwan Ratnayake, M.O. Schrenk, E.M. Schwarzenbach, K.I. Twing, D. Weis, S.A. Whattam, M. Williams, and R. Zhao²

Keywords: International Ocean Discovery Program, IODP, *RRS James Cook*, Expedition 357, Site M0068, Site M0075, seabed drills, RD2, MeBo, Atlantis Massif, Atlantis Fracture Zone, Mid-Atlantic Ridge, Lost City hydrothermal field, serpentinization, detachment faulting, oceanic core complex, hydrogen, methane, deep biosphere, carbon cycling, carbon sequestration, contamination tracer testing

Contents

- 1 Operations
- 3 Lithology, alteration, and structure
- 15 Bulk rock geochemistry
- 20 Fluid chemistry
- 23 Microbiology
- 24 Sensor package data
- 29 Physical properties
- 28 Borehole plugs
- 32 Downhole logging
- 34 Paleomagnetism
- 35 References

Operations

During Expedition 357, cores were recovered from two sites in the eastern area of Atlantis Massif: Sites M0068 and M0075 (Figure [F1](#); Table [T1](#)). Newly acquired multibeam data, combined with pre-existing data sets, were evaluated prior to each site to guide the drill teams with regard to anticipated seabed conditions and slope.

Site M0068

Cores were recovered from two holes at Site M0068 (proposed Site AM-02A), with an average site recovery of 58.88%. The mean water depth for the two holes was 1102.35 m with no tidal range. The total time spent on station was 2.36 days.

Hole M0068A

The *RSS James Cook* moved onto Site M0068 at 2208 h on 5 November 2015, with the site position centered over the British Geological Survey RockDrill2 (RD2) port-side deployment position. The vessel settled into dynamic positioning (DP) mode. Prior to coring at each location, a conductivity, temperature, and depth (CTD) cast was conducted to quantify the background geochemistry and microbiology within the water column. The CTD was deployed at 2248 h and held at 10 m water depth for a full systems check. At 2332 h, the CTD was 1.6 m off the bottom, and the first three Niskin bottles were fired. Two more Niskin bottles were fired on the way up, with a final one fired near the surface (see Table [T5](#)

in the Expedition 357 summary chapter [Früh-Green et al., 2017c]). The CTD was recovered to deck at 0005 h on 6 November.

During the ship CTD cast, the RD2 was made ready for deployment, but a communications problem with the CTD sensor mounted on the drill delayed launch. The RD2 was deployed at 0124 h; however, problems with the winch spooling mechanism and the methane sensor on the water sensor package meant the drill was recovered at 0146 h before landing on the seafloor. At 0234 h, the RD2 was launched again, landing on the seafloor at 0356 h after a full mid-water column systems check. Coring operations commenced at 0418 h.

The first core run was completed at 0602 h. However, a problem with the arm shift meant the RD2 had to be recovered after a total penetration of 1.97 m. Prior to recovery, the Niskin bottles on the water sampling package were fired. The RD2 was on deck and secure by 0835 h. The vessel began to transit to Site M0069 at 0840 h on 6 November. Preparations began for deploying the Meeresboden-Bohrgerät 70 (MeBo) drill.

One coring attempt was made in Hole M0068A to a maximum depth of 1.97 m with 23.92% recovery.

Hole M0068B

The vessel arrived on station at 1545 h on 23 November 2015. RD2 preparations continued until 1757 h, when the drill was deployed. At 1836 h, the RD2 was brought back on deck after a mid-water column systems check revealed two sensor inputs were

¹ Früh-Green, G.L., Orcutt, B.N., Green, S.L., Cotterill, C., Morgan, S., Akizawa, N., Bayrakci, G., Behrmann, J.-H., Boschi, C., Brazelton, W.J., Cannat, M., Dunkel, K.G., Escartin, J., Harris, M., Herrero-Bervera, E., Hesse, K., John, B.E., Lang, S.Q., Lilley, M.D., Liu, H.-Q., Mayhew, L.E., McCaig, A.M., Menez, B., Morono, Y., Quéméneur, M., Rouméjon, S., Sandaruwan Ratnayake, A., Schrenk, M.O., Schwarzenbach, E.M., Twing, K.I., Weis, D., Whattam, S.A., Williams, M., and Zhao, R., 2017. Eastern sites. In Früh-Green, G.L., Orcutt, B.N., Green, S.L., Cotterill, C., and the Expedition 357 Scientists, *Atlantis Massif Serpentinization and Life*. Proceedings of the International Ocean Discovery Program, 357: College Station, TX (International Ocean Discovery Program). <http://dx.doi.org/10.14379/iodp.proc.357.103.2017>

² Expedition 357 Scientists' addresses.
MS 357-103: Published 4 February 2017

Figure F1. Detailed site and hole location images for Sites (A) M0075 and (B) M0068 overlain onto DSL120 sonar imagery (from Blackman et al., 2002) in two different swath orientations and the newly acquired 50 m resolution multibeam bathymetry.

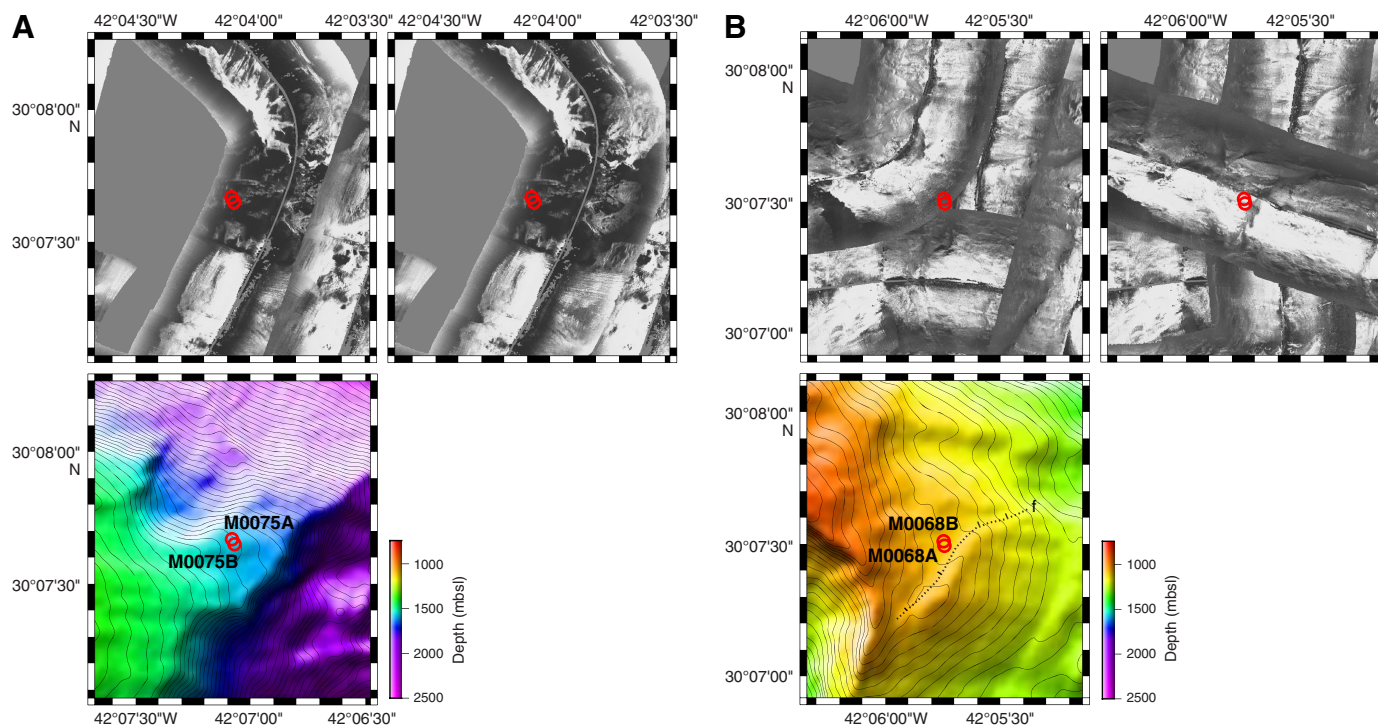


Table T1. Eastern sites hole summary. [Download table in .csv format.](#)

| Date coring operations commenced (2015) | Hole | Proposed site | Latitude | Longitude | Water depth (m) | Drill | Number of cores | Interval cored (m) | Core recovered (m) | Core recovery (%) | Interval open holed (m) | Penetration depth (mbsf) | Time on site (days) |
|---|--------|---------------|-----------|-----------|-----------------|-------|-----------------|--------------------|--------------------|-------------------|-------------------------|--------------------------|---------------------|
| 5 Nov | M0068A | AM-02A | 30°7.493N | 42°5.743W | 1102.70 | RD2 | 1 | 1.97 | 0.47 | 23.92 | 0.00 | 1.97 | 0.41 |
| 23 Nov | M0068B | AM-02A | 30°7.51N | 42°5.747W | 1102.00 | RD2 | 9 | 11.25 | 6.34 | 66.04 | 0.00 | 9.60 | 1.95 |
| 28 Nov | M0075A | AM-03A | 30°7.669N | 42°3.981W | 1568.00 | RD2 | 1 | 1.72 | 0.65 | 37.79 | 0.00 | 1.72 | 0.57 |
| 29 Nov | M0075B | AM-03A | 30°7.65N | 42°3.97W | 1568.00 | RD2 | 3 | 5.70 | 2.73 | 47.88 | 0.00 | 5.70 | 1.10 |

wrongly connected. The RD2 returned to deck at 1848 h and was back in the water again by 1900 h. At 2012 h, the RD2 landed on the seafloor but had to be repositioned due to the high tilt angle of the drill. At 2031 h, the RD2 was settled on the seafloor, and coring operations began at 2051 h. The first four core runs were completed at 2250 h on 23 November and 0213, 0702, and 1158 h on 24 November. Following a problem with the LED power supply, the tracer injection system was turned off from 0744 to 1423 h on 24 November, covering the period of core Run 4. The fourth core barrel was stuck in the bottom-hole assembly (BHA), so the entire BHA was tripped and a new one was inserted with a G7 bit.

Difficulty was noted on reaming back down the hole, and coring had to start from 1 m above the base of the hole because it looked like the hole had partially collapsed. Core Run 5 started at 1452 h and was completed by 1605 h. At 1800 h, a hydraulic oil leak from the top drive was noted. At the rate of loss, there was approximately 20 h coring time left before logging and installing the borehole plug would have to take place. Core Runs 6 and 7 were recovered at 1908 h and 2340 h, respectively. Core Run 7 did not achieve full penetration. Core Run 8 began at 0037 h on 25 November, but by 0618 h, little progress (≈ 0.7 m) had been made, so the barrel was tripped

and the hole conditioned and reamed. Barrel 9 was then loaded. However, after a discussion about the hole conditions, we decided to abandon the hole and attempt logging and installation of the borehole plug.

During this discussion, it was noted that the flush was variable with difficulties maintaining the flush pressure and flow; it was found that the barrel was stuck in the BHA. At 1034 h the optical-acoustic-gamma (OAG) logging tool was deployed, conducting two through-pipe upward logging passes, as described in [Downhole logging](#). These passes were completed by 1046 h. The magnetic susceptibility tool was then deployed (at 1136 h) through the pipe as an operational test for deployment, triggering, and recovery because this had not been done so far on the expedition. The test was successfully completed by 1213 h. At 1218 h, tripping of the rods commenced.

Installation of the downhole plug commenced at 1305 h and was completed by 1343 h; more details on the installation are available in [Borehole plugs](#). As the RD2 lifted off the seafloor at 1350 h, the rig tilted and caught the top of the plug with the breakout table. It is unknown whether the plug was fully or partially pulled out of the borehole. The RD2 was recovered to deck and secure by 1434 h on

25 November, and the vessel immediately began to transit toward Site M0071.

In summary, nine coring attempts were made in Hole M0068B to a maximum depth of 9.60 m with 66.04% recovery.

Site M0075

Cores were recovered from two holes at Site M0075 (proposed Site AM-03A), with an average site recovery of 45.46%. The water depth was 1568.00 m with no tidal range. An additional CTD cast that was conducted over the Mid-Atlantic Ridge was linked to this site (Hole M0075X). The water depth at this location was \approx 4222 m. The total time spent on station was 1.67 days.

Hole M0075A

At 0300 h on 14 November 2015, the vessel turned onto an east-southeast course for Site M0075. The vessel settled into DP mode at 0800 h; however, the swell (>4 m) was prohibitive for the deployment of either drill. At 0838 h, a CTD cast was begun. At 1003 h, the CTD was 2.4 m off the bottom and the first three Niskin bottles were fired. Two further Niskin bottles were fired on the way up, with a final one fired near the surface (see Table T5 in the Expedition 357 summary chapter [Früh-Green et al., 2017c]). The CTD was recovered on deck by 1102 h. Having completed the CTD, the sea state was still too rough to deploy either drill, so the vessel moved off site at 1111 h on 14 November to conduct an additional CTD cast over the Mid-Atlantic Ridge (Hole M0075X).

The vessel returned to Site M0075 on 28 November at 0625 h from Hole M0071C. The RD2 was initially deployed at 0654 h. However, after repositioning three times because of the angle of the rig on landing, the RD2 had to return to deck at 0912 h because of a minor oil leak. The RD2 was redeployed at 1058 h and landed on the seafloor at 1153 h. Coring commenced at 1210 h, and the first core run was completed by 1320 h. Core Barrel 2 was loaded into the BHA at 1356 h, but at 1400 h, the RD2 suffered a sensor cable fault and we had to abandon the hole, returning the drill to deck at 1500 h. The vessel held position for rig repairs. By 1700 h, the cable was changed out, but a hydraulic leak in the top drive was discovered. The only option was to exchange the top drive for another one, which would take approximately 18 h. The fault with the MeBo, suffered during Hole M0071C operations immediately prior to Hole M0075A operations, was a hydraulic slip ring inside the top drive assembly that was not repairable at sea, so the MeBo could not be deployed. Because repairs to the RD2 would take some time, we decided to leave the site and continue running the multibeam survey. The vessel departed the site at 2013 h on 28 November.

In summary, one coring attempt was made in Hole M0075A to a maximum depth of 1.72 m with 37.79% recovery.

Hole M0075B

The vessel arrived on station at 0725 h on 29 November 2015 having completed a short multibeam survey at 0547 h. Repairs were still ongoing on the RD2, so the vessel waited on station until the drill was ready for deployment at 1505 h. During mid-water column checks, a misalignment between the newly fitted top drive and the breakout table was noted, and the RD2 was recovered on deck at 1540 h. The RD2 crew removed the shims from the breakout table and redeployed at 1834 h despite a small misalignment. The RD2 landed on the seafloor at 1941 h and began coring operations at 1948 h. The first core was recovered at 2028 h. The second barrel was inserted, and a rod was added. The misalignment meant that this previously automated action had to be done manually after the

first automated attempt resulted in the threads of the rod being ripped off. This situation meant longer rod handling times but allowed coring to continue despite the misalignment.

Core Run 2 was completed at 2329 h, and a new core run commenced at 0015 h on 30 November. At 0530 h, there was a technical failure in the electronic control module (ECM), terminating the hole and preventing any logging runs because we were unable to operate the overshot. The Niskin bottles on the sensor package were fired at 0612 h, the drill rods and BHA were recovered to the rig by 0652 h, and a shortened version of the downhole plug was installed by 0845 h (details of the installation are available in [Borehole plugs](#)). The RD2 was back on deck and secure by 0950 h on 30 November, and the vessel departed for Site M0074 immediately.

In summary, three coring attempts were made in Hole M0075B to a maximum depth of 5.70 m with 47.88% recovery.

Lithology, alteration, and structure

Sites M0068 and M0075 are the easternmost sites drilled along the east–west transect of the Atlantis Massif southern wall (Figure F2). Two holes were drilled at both sites, the first of each recovering predominantly surficial sedimentary material (Figure F3). Hole M0075A is very shallow; it was drilled to 1.72 mbsf with 0.65 m of rock recovered. Hole M0075B was drilled to 5.7 mbsf and recovered 2.73 m of core. Hole M0068A is also very shallow, with 0.47 m core

Figure F2. High-resolution multibeam bathymetry showing drilling locations. Contour interval = 20 m. A. Holes M0075A and M0075B. B. Holes M0068A and M0068B and an oblique fault (dashed line; tick marks on hanging wall [f]) cutting the striated detachment fault surface.

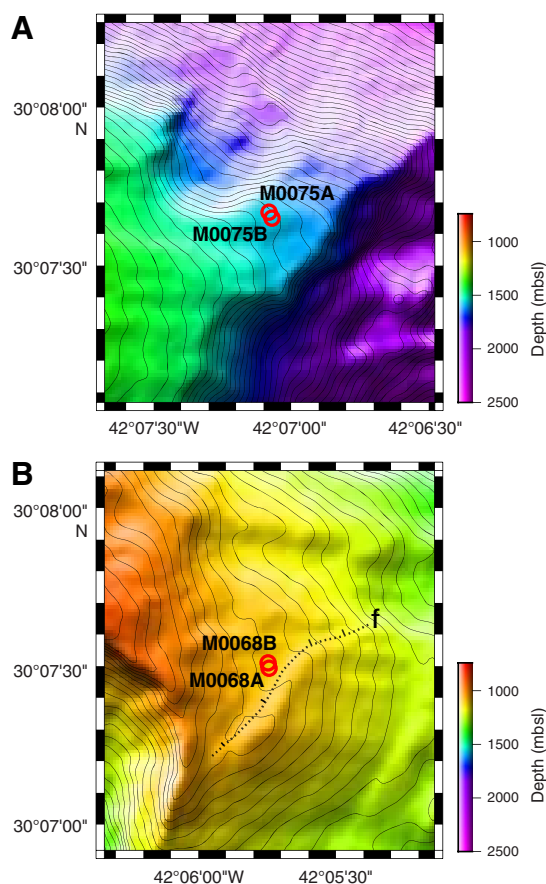
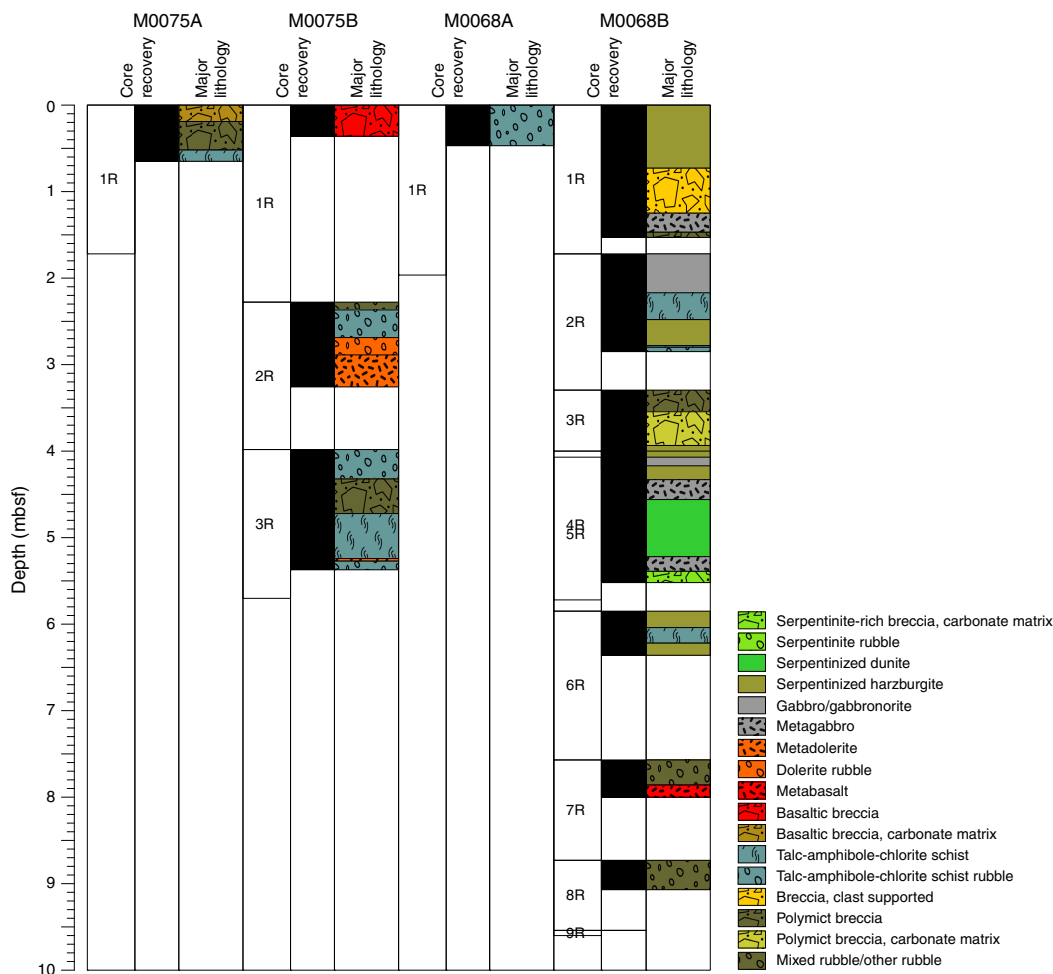


Figure F3. Lithologic summary for eastern holes, Expedition 357.



recovered. Hole M0068B extends to 9.6 mbsf and recovered 6.34 m of core (66% recovery).

The tops of both holes at Site M0075 are composed of sedimentary breccia with a carbonate matrix. This breccia includes fragments of unaltered basalt (Hole M0075B) or metabasalt and serpentinite fragments (Hole M0075A). The breccia is matrix supported and undeformed and contains foraminifers within the matrix. In Hole M0075B, the breccia exhibits a horizon with smaller clasts showing distinct subhorizontal layering. Because Hole M0075A solely contains this sedimentary material, the following descriptions only concern Hole M0075B.

In Hole M0075B, a transition occurs in the sedimentary breccia unit around 0.16–0.19 mbsf (Core 1R) between the uppermost level, which contains pale brown (oxidized) foraminiferal carbonate matrix and angular clasts composed of metabasalt, and the lower level, which contains clasts dominantly composed of schistose talc-bearing ultramafic material. These clasts are occasionally aligned and define rough horizontal layering. The matrix is pale yellow to green. Core 2R contains a rubbly unit (sand and fragments <4 cm) of angular and schistose fragments, some composed principally of talc and serpentine but most with significant amounts of amphibole and chlorite. This rubbly material is locally enclosed in pale green unconsolidated mud predominantly composed of talc and chlorite. Rubble with a pale green sandy matrix and mud are found in inter-

vals 2R-1, 13–36 cm, and 3R-1, 32–53 cm, and likely extend to 74 cm in the sample taken for microbiology. The origin of these sandy intervals is unclear. Between the two intervals in Cores 2R and 3R are larger loose fragments of metadolerite and talc-bearing ultramafic rocks. Metadolerites show cataclastic deformation under greenschist facies conditions but no foliation. Below the second sandy interval (below Section 3R-1, 126 cm) to the bottom of the hole (interval 3R-CC, 102–109 cm; 5.37 mbsf), a unit of amphibole-chlorite schist with minor talc shows subhorizontal to moderately dipping foliation and two intervals of cataclastically deformed (but not schistose) metadolerite. This lowest interval of schist and metadolerite appears to be in situ and not from rubble.

Hole M0068A cores contain several fragments with two types of lithology: talc-overprinted serpentinitized peridotite and amphibole-chlorite-bearing fragments that may be metadoleritic. Several of these fragments are schistose with well-defined foliation. Several fragments are encrusted with carbonate sediment, and the biggest piece (1R-1 [Piece 3]) bears a thin coating of iron-manganese oxides. The most probable interpretation is that this piece is sedimentary rubble.

The top of Hole M0068B (Cores 1R–4R; 0–5.39 mbsf) contains long, continuous pieces with variable lithology: serpentinitized harzburgite, talc-bearing serpentinitized harzburgite, talc-bearing serpentinitized harzburgite with intervals that contain amphibole and

chlorite (which may have been mafic intrusions), and metagabbro. Massive metagabbro with very limited subsolidus deformation occurs in several intervals: 1R-1, 127–139 cm, 2R-1, 0–44 cm, and 4R-1, 125–139 cm. Loose rubble including fragments of sheared gabbro occurs in interval 3R-1, 0–15 cm. Several intervals consist of serpentized harzburgite with variable proportions of talc or irregular patches of probable gabbroic material, commonly bearing zircon. These patches are typically foliated (an example is found in the form of a subvertical shear zone in a probable altered gabbroic vein in interval 1R-1, 44–68 cm). Altogether, intervals of serpentized peridotites that have been neither metasomatized into talc-rich assemblages nor infiltrated by gabbroic material are rare: intervals 1R-1, 35–50 cm, and 4R-1, 60–90 cm.

The long pieces of coherent hard rock in Cores 1R–4R are interspersed with several intervals of consolidated breccia: 1R-1, 52–61 and 69–93 cm, 3R-1, 19–46 cm, and 4R-CC. This breccia has a carbonate matrix and angular fragments of variably oxidized serpentized ultramafic rocks, talc-bearing serpentized ultramafic rocks, metadolerites, and metagabbros. Foraminifers are not apparent in the matrix. The presence of this breccia can be interpreted in three ways: (1) the drilled formation to at least the bottom of the deepest breccia interval (0–5.52 mbsf) is composed of large mass-wasted blocks; (2) the drilled formation is overall in situ but has been subjected to seafloor weathering and fracturing, with sediment and breccia falling between fractures and filling voids adjacent to disjointed but not substantially displaced blocks; or (3) the breccia is not sedimentary but represents highly cataclastic intervals that are part of the fault deformation history.

Interpretation 3 is not favored based on the lack of macroscopically visible deformation in the breccia and at its contacts with the coherent rock intervals. Whether Interpretation 1 or 2 is correct has significant consequences to the way the core is interpreted. If Interpretation 2 is correct, the lithologic and structural relationships summarized above and described in more detail in the following sections largely reflect the original relations. If Interpretation 1 is correct, the original lithologic relations are not preserved, except for those that occur within coherent pieces of core, and the orientation of the structures in the core does not reflect protolithic or exhumational deformational processes. No clear observational evidence was found in the upper cores to defend either interpretation. However, the rubbly nature of the formation drilled below Core 4R and the location of Hole M0068B at the base of a small fault scarp (Figure F2) are two indications in favor of Interpretation 1.

Below Core 4R (5.39 mbsf to the bottom of the hole at 9.07 mbsf), drilling recovered only loose rubble. The material in Core 5R likely represents debris accumulated in the hole during drill string pullout (see **Operations**), whereas the rubble in Cores 6R–8R comes from the corresponding drilled interval (5.85–9.07 mbsf). The rubble pieces are typically 3–6 cm in size, and several exhibit traces of drilling and redrilling. It is likely that either the formation was itself loose rubble or that it comprised relatively competent clasts in a noncohesive matrix. The rock types are different from those in Cores 1R–4R. Pebbles of variably oxidized talc-bearing serpentized peridotite and amphibole-talc-chlorite schist occur in Core 6R and the uppermost 16 cm of Core 7R. Several fragments have the shape of sheared phacoids. The bottom of Cores 7R and 8R also contain shattered pieces of dolerite.

Site M0075

Rock types and igneous petrology

Hole M0075A

Core 1R consists of two units of carbonate-rich sedimentary breccia with angular clasts (up to 5 cm) mainly consisting of basalt and foliated talc-rich rocks (Unit 2).

Hole M0075B

The top of Core 1R also comprises carbonate-rich sedimentary breccia with two angular 5–6 cm clasts of basalts.

Unit 3 (Section 2R-1) contains loose pebbles of metadolerite and possibly metagabbroic material. Unit 4 comprises a coherent piece of metadolerite (7 cm) and several pieces of deformed metadolerite. The interval taken for shipboard microbiology sampling likely also consists of metadolerite rubble, and the core catcher contains pebbles as large as 5 cm of fine-grained metadolerite. A thin section (Sample 2R-1, 64–66 cm) confirms heavy alteration ($\approx 85\%$) in the dolerite matrix, but primary textural relationships are still observable. The primary mineralogy consists of remnants of lath-shaped, subhedral, and corroded plagioclase (20%; up to 1 mm) along with minor oxides; clinopyroxene is completely altered.

Core 3R is dominated by chlorite-amphibole schist except for Unit 4, which consists of a coherent piece of fine-grained aphyric metadolerite with chilled margins. One chilled margin is observed along the edge of a piece of metadolerite within chlorite-amphibole schist (interval 3R-1, 74–126 cm) (Figures F4, F5). The metadolerite is pale green with a dark green chilled margin cut by chlorite veins.

Figure F4. A. Metadolerite cutting an amphibole-chlorite schist (357-M0075B-3R-1, 100–102 cm; cross-polarized light [XPL]). An internal intrusive contact in the dolerite is cut by small faults that are localized undeformed chlorite (Chl) veins. B. Close-up of an undeformed chilled margin of the dolerite dike cutting schistose tremolite. Coarser parts of the dike show plagioclase laths with clinopyroxene altered to amphibole.

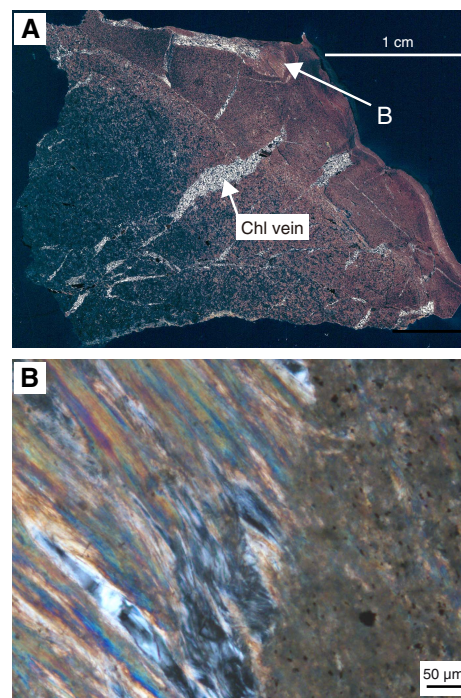
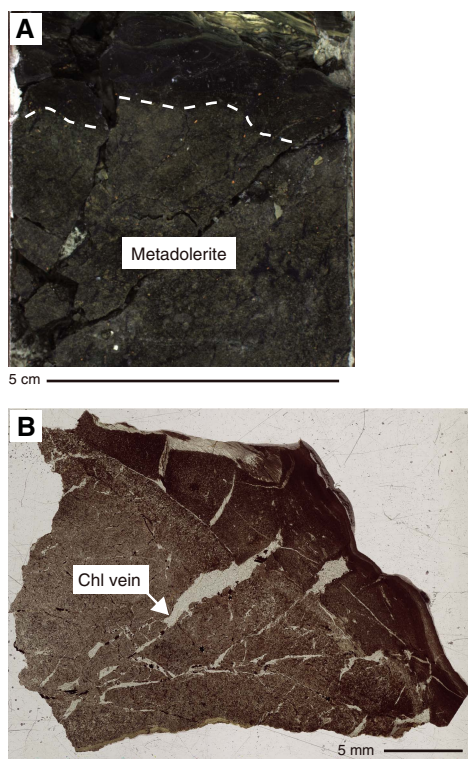


Figure F5. A. Chilled margin of metadolerite in hand sample (357-M0075B-3R-1, 100–106 cm). Dashed line = chilled margin confirmed by microscopic observation. B. Thin section of chlorite vein (3R-1, 100–102 cm; plane-polarized light [PPL]).



Alteration

The lithologies present at Site M0075 are mostly composed of sedimentary breccia to rubble intervals with a transition from basalt to amphibole-chlorite- and talc-chlorite-bearing clasts. All of the clasts and rubble underwent variable alteration prior to the formation of breccia. The basaltic clasts (intervals 357-M0075A-1R-1, 0–20 cm, and 357-M0075B-1R-1, 12–40 cm) are slightly altered with dark gray background alteration with orange alteration halos around the exterior edges (up to 5 mm). Metadolerite in a rubble section (interval 2R-1, 46–66 cm) is moderately altered with green background alteration and rare dark alteration halos. In thin section, amphibole and chlorite are observed replacing clinopyroxene, and chlorite also replaces plagioclase. Within Hole M0075B, pale green talc-amphibole-chlorite schists are present as rubble and as clasts within a breccia. X-ray diffraction (XRD) and thin section analyses indicate that the assemblage is dominated by talc and chlorite. The base of Hole M0075B (Section 3R-1) consists of a mafic unit dominated by talc-amphibole-chlorite schist intruded by dolerite dikes that exhibit a range of colors from yellow-green to dark gray-green (see VCDs in [Core descriptions](#)). XRD analyses of Sample 3R-1, 78–86 cm, indicate that the secondary mineral assemblage is dominated by amphibole and chlorite.

Veins and crosscutting relationships

Veins within the coherent core intervals include serpentine veins with carbonate cores (Section 357-M0075A-1R-CC). In Hole M0075B, veins are generally <1 mm thick with variable shades of green. The metadolerite in Sample 2R-1, 64–66 cm, hosts a 1 mm quartz vein with a chlorite-rich alteration halo and 0.2 mm wide saponite ± iron oxyhydroxide veins that transition into chlorite as they

Figure F6. Background alteration of dolerite to chlorite cut by a quartz vein with a chlorite-rich alteration halo (357-M0075B-2R-1, 64–66 cm). Toward the alteration halo, thin veins change composition from iron-oxyhydroxide dominated to chlorite dominated.



pass into the chlorite-rich halo (Figure F6). Also present is a sub-parallel, irregular 0.1 mm quartz vein that hosts zircon crystals.

Structure

Site M0075 is located over the striated surface along the easternmost part of the southern ridge of Atlantis Massif. The two holes (Hole M0075A cored depth = 0.65 mbsf; Hole M0075B = 5.7 mbsf) were drilled near the present-day rift valley wall that cuts the detachment fault surface at its eastern limit. There, the bathymetry shows a gentle slope of <math><10^\circ</math> toward the ridge axis, and the sites are located in a narrow apron extending northeastward, with mass-wasting scarps north and south of the site (Figure F2).

We identified the same three structural intervals in Holes M0075A and M0075B, and the upper two breccia units were found in both holes. The lower structural interval was only drilled in Hole M0075B.

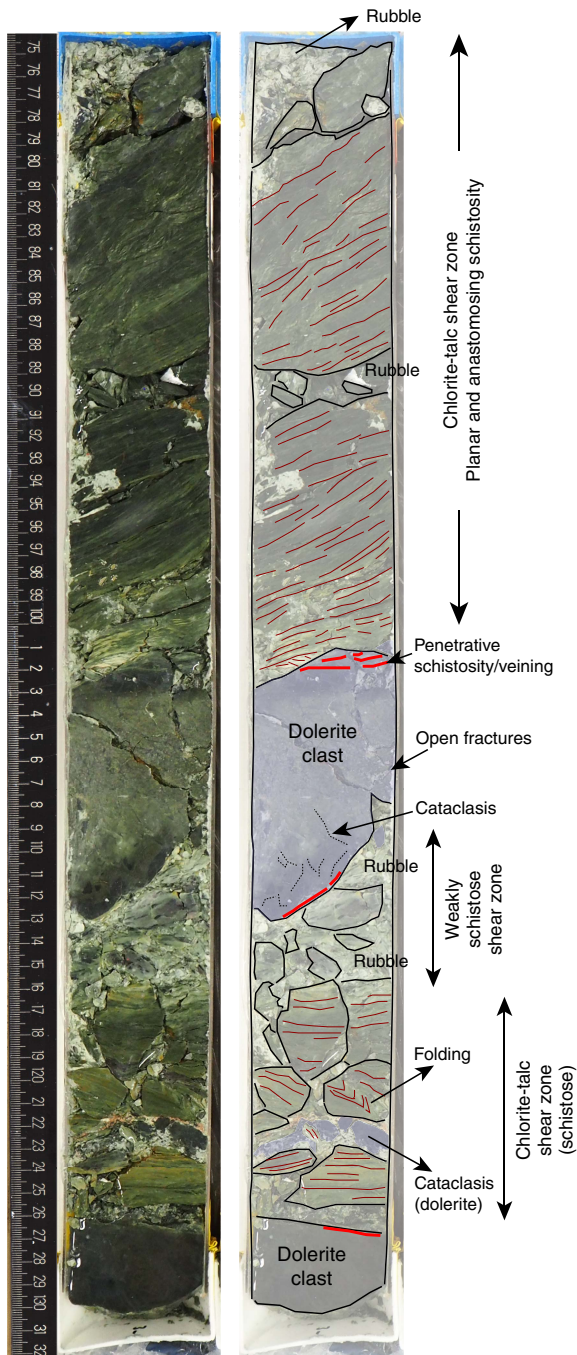
Breccia

Holes M0075A and M0075B both cored intervals of matrix-supported breccia up to ≈ 20 cm thick. The matrix is sandy carbonate sediment supporting large angular clasts (some ≥ 5 cm) composed primarily of metabasalt. The matrix shows no deformation structures. The lower breccia interval, extending to ≈ 2.6 mbsf, was cored in Hole M0075B and at the bottom of Hole M0075A (to ≈ 0.65 mbsf). In contrast to the breccia above, this interval is clast supported and hosts smaller clasts (up to 1–2 cm) with both angular and elongated shapes that correspond in general to metabasaltic and schistose rock types, respectively. The foliation intensity in the schistose clasts is high and likely defined by talc and possibly tremolite. The lower breccia shows weak alignment and imbrication of elongated clasts that impart poorly developed subhorizontal layering. The matrix is pale green and shows no deformation structures (see VCDs in [Core descriptions](#)).

In Section 357-M0075B-3R-1, 75–132 cm (4.71–5.28 mbsf), a depositional contact exists between this lower breccia and a ≈ 60 cm thick shear zone hosting a complex internal structure (Figure F7) that corresponds to the lowest structural interval. The core of the fault zone is generally structurally continuous (with narrow intervals of rubble) and displays several elements that characterize its internal architecture (from top to bottom, but overlapping):

- Dark green talc-chlorite schist (interval 1R-1, 75–101 cm) hosts well-developed planar and anastomosing schistosity and records high-strain deformation. The upper ≈ 25 cm of this unit corresponds to a continuous section with gently dipping ($\approx 20^\circ$) folia-

Figure F7. Structural interpretation and units found within the fault zone (357-M0075B-3R-1, 75–132 cm).



tion, and the lower ≈ 10 cm is shattered (probably by drilling) but likely in situ and shows subhorizontal foliation.

- A deeper zone of highly fractured core (interval 1R-1, 110–116 cm) with variable thickness (≈ 4 –6 cm) in the lower part of the fault zone hosts lighter green clasts with a mottled texture (dark, irregular areas with diffuse boundaries) and very weak or no foliation. Clasts of similar appearance in the overlying rubble are talc rich.
- The deepest recovered section includes metadolerite (main clasts at 1R-1, 101–110 and 126–130 cm) either as large clasts within the schistose fault material (≈ 10 and ≈ 5 cm) or as zones

as thick as 2 cm showing intense cataclastic deformation of dolerite clasts stretched parallel to the overall schistosity. The larger clasts show schistose green material at their edges and green veins penetrating along their margins (thick red lines in Figure F7). The larger dolerite clasts also show early cataclasis in the form of small fractures and possible veins, likely occurring prior to the deformation associated with the main shear zone described here. One preserved contact between dolerite and schist hosts a chilled margin to the dike (Figure F4), highlighting the relationship between intrusion, deformation, and metamorphism within the fault zone. This fault zone thus records ductile deformation of schistose intervals, possibly repeated intrusion of dolerite, and brittle deformation of all units that host heterogeneous cataclastic deformation reworked within the shear zone.

Site M0068

Rock types and igneous petrology

Site M0068 comprises two holes, M0068A and M0068B, and only the latter contains relict igneous rocks. Eight cores were recovered from Hole M0068B. A summary of igneous petrological features is presented below, and downhole lithologic variations are depicted in Figure F8 (see VCDs in **Core descriptions**).

Section 357-M0068B-1R-1 comprises five lithologic units that consist mainly of serpentinized porphyroclastic harzburgites (Units 1, 2, and CC). The harzburgites occasionally exhibit mesh textures and contain porphyroclasts (bastite after orthopyroxene; 2–10 mm). Units 3 and 4 are carbonate- and talc-amphibole-chlorite-hosted breccia. Unit 3 is polymict with angular clasts (a few millimeters to a few centimeters) of metabasalt and talc schist. The clasts in Unit 4 are mostly talc-amphibole schists. The metagabbro in Unit 5 is coarse grained and consists of subhedral, <0.5 –4 mm plagioclase laths (50%); 2–3 mm equant, subhedral clinopyroxene (35%); brown amphibole ($<15\%$); and oxides ($<1\%$) (interval 1R-1, 134–139 cm). The core catcher contains unconsolidated breccia with angular fragments of mostly serpentinized harzburgite. The larger fragments (up to 5 cm) exhibit mesh texture.

Section 2R-1 comprises an uppermost 45 cm interval of slightly deformed but relatively fresh gabbro (Unit 1) and an approximately 40 cm thick unit of pyroxene-poor ($<10\%$; post-serpentinization) serpentinized harzburgite (Unit 3) overprinted by talc, chlorite, and amphibole. Units 1 and 3 are separated by talc-amphibole-chlorite schist. Gabbro is generally coarse grained but exhibits gradation in plagioclase grain size (from 10 to 1 mm) toward the bottom of the interval. The gabbro is dominated by subhedral to anhedral plagioclase ($<70\%$; average grain size = 10 mm); clinopyroxene (up to ≈ 3 mm) and orthopyroxenes (up to ≈ 3 mm) are present in modal abundances of $\approx 10\%$ and $\approx 5\%$, respectively (interval 2R-1, 31–36.5 cm). Pyroxenes are interstitial to plagioclase grains. Some clinopyroxenes enclose subhedral tabular plagioclase grains. Serpentinized harzburgite (Unit 3) is oxidized and locally altered to talc, chlorite, and amphibole (as seen in interval 2R-1, 78–85 cm) (Figure F9). The serpentinized harzburgite also contains relict orthopyroxene (3–6 mm bastites with a modal abundance of 5%–10%), chromian spinel grains, and relict mesh texture outlined by magnetite concentrations.

Unit 1 of Section 3R-1, 10–25 cm, consists of subrounded to subangular fragments of multiple rock types (up to 4 cm), including metagabbro and serpentinized porphyroclastic harzburgites. Unit 2 is carbonate-hosted, loosely consolidated breccia with angular to subrounded clasts of serpentinized harzburgite and talc-amphibole

Figure F8. Alteration, Hole M0068B. Alteration intensity: 0 = fresh (<2%), 1 = slight (2%–20%), 2 = moderate (21%–40%), 3 = high (41%–80%), 4 = very high (81%–95%), 5 = total (>96%). Distribution of alteration types: 1 = pervasive, 2 = localized, 3 = patchy.

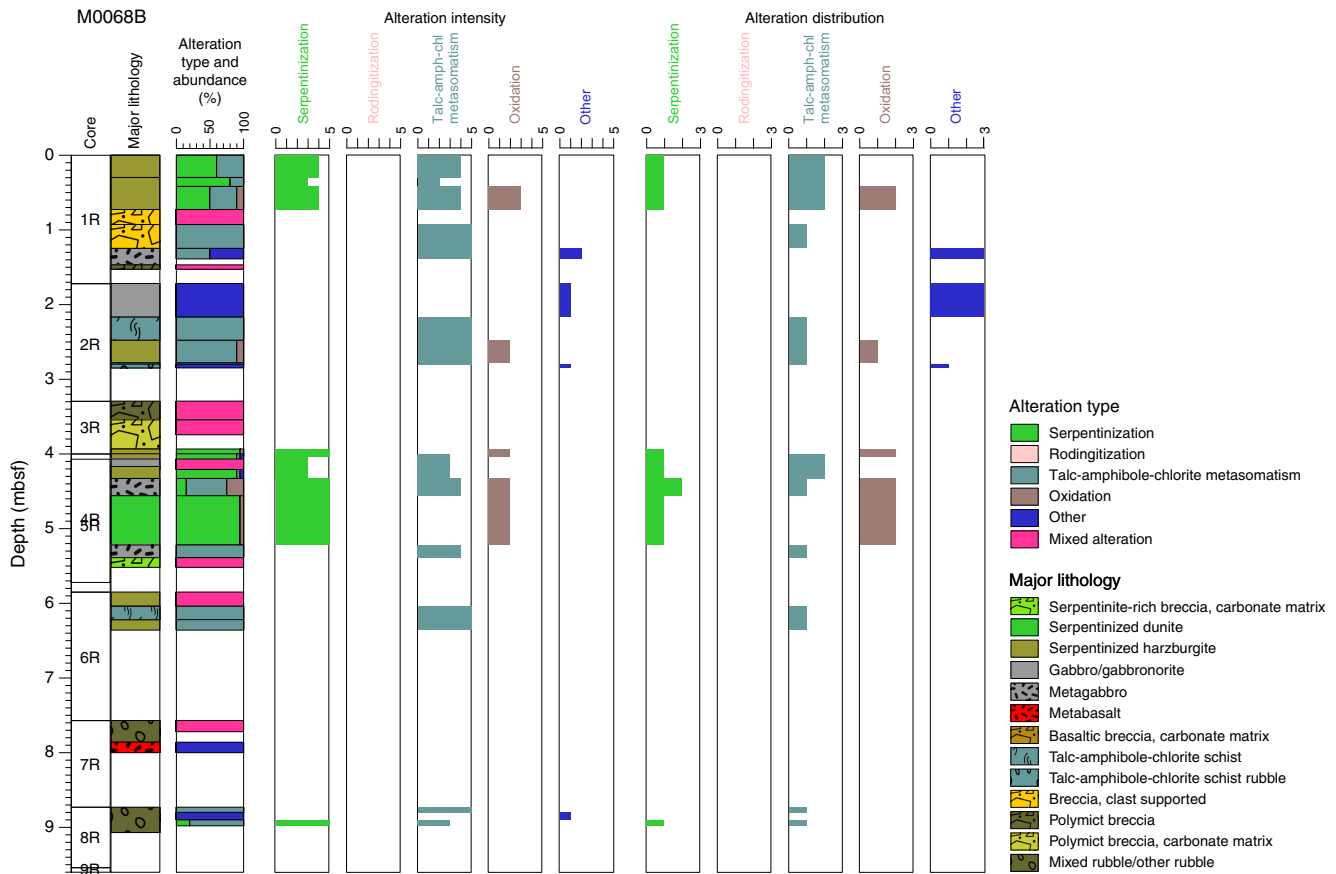
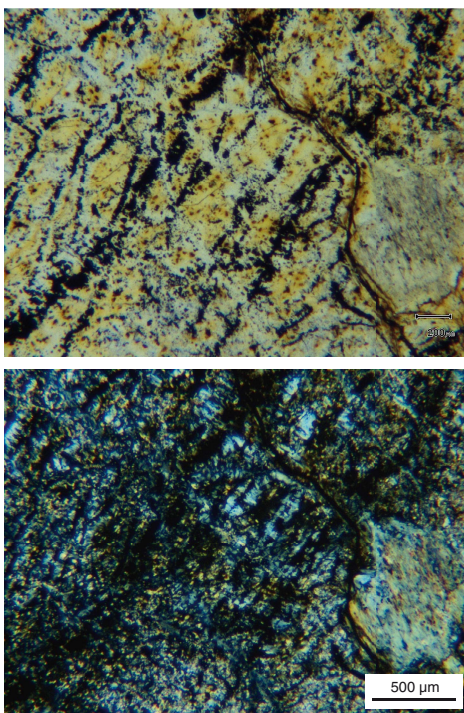


Figure F9. Talc replacement of mesh texture and alteration of pyroxene (357-M0068B-2R-1, 78–85 cm).



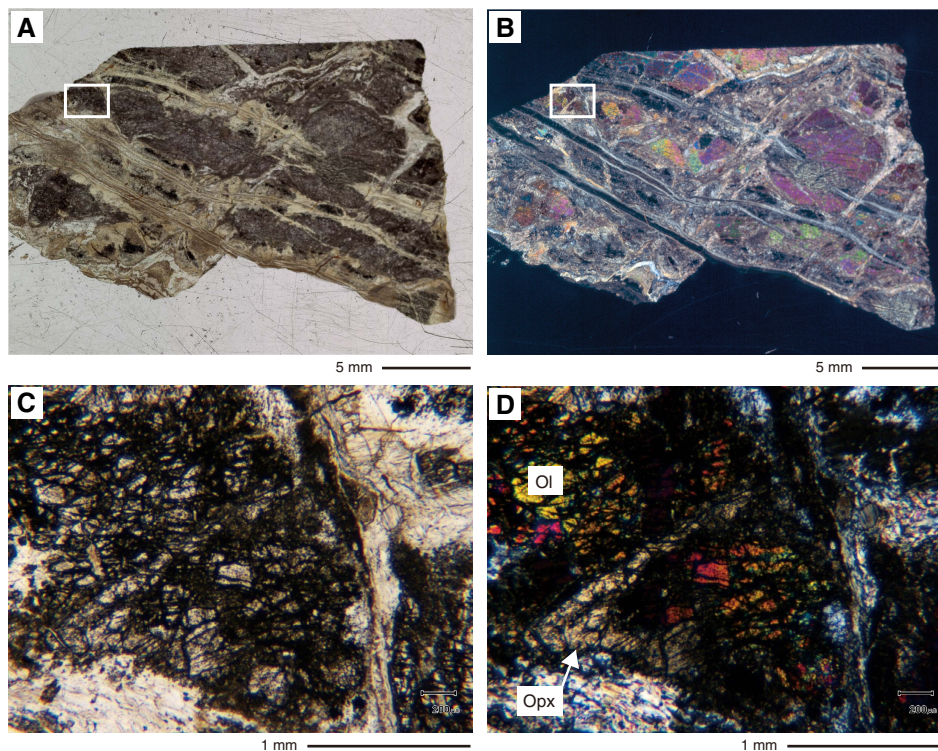
schist. The core catcher consists of serpentinized porphyroclastic harzburgite with rounded to subrounded porphyroclasts (bastites up to 5 mm in diameter).

Section 4R-1 consists of serpentinized peridotite and metagabbro. Unit 1 (0–17 cm) comprises rubble composed of fragments (up to 6 cm) of serpentinized porphyroclastic harzburgite. The underlying unit consists of serpentinized harzburgite locally impregnated by thin gabbroic veins. This interval locally contains fresh olivine and deformed relict orthopyroxene that exhibits undulose extinction; plagioclase was also observed but is mostly altered to chlorite (interval 4R-1, 18–22 cm). The metagabbro of Unit 3 is approximately 3 cm thick and intrudes into serpentinized peridotite. Unit 4 is a homogeneous sequence of serpentinized dunite (no bastite visible) cut by two sets of veins subparallel to the fabric. Unit 5 is composed of metagabbro exhibiting pseudomorphs after coarse pyroxenes within the outer sections of a zoned metasomatic interval. Section 4R-CC contains fragments of serpentinized porphyroclastic harzburgite in a carbonate-dominated matrix (see VCDs in [Core descriptions](#)).

Section 5R-1 consists of serpentinized porphyroclastic harzburgite rubble and some metagabbroic fragments. The metagabbro is medium grained and varitextured and consists of 5–10 mm tabular, lath-shaped plagioclase (25%) and 3–5 mm stubby, anhedral, and subrounded clinopyroxene (40%).

Section 6R-1 recovered only rubble, with three units distinguished based on changes in lithology. Units 1 and 3 contain subrounded pebbles of serpentinized harzburgites (10% modal

Figure F10. Serpentinized dunite (357-M0068B-4R-1, 50–53 cm). A, B. Scan of thin section (PPL). C, D. Orthopyroxene (Opx) vein cutting olivine (Ol) grain (XPL). Position is shown by white squares in A and B.



abundance of 3–5 mm remnants of orthopyroxenes) and altered dolerite/gabbro. Unit 2 consists of angular fragments of talc-amphibole-chlorite schist with one clast containing undeformed fine-grained mafic material that may be interpreted as a dike margin.

Section 7R-1 is composed of two units. Unit 1 is mixed rubble containing several pieces of mafic to ultramafic fault rocks, including breccia fragments, metagabbro, and dolerite. Unit 2 contains fragments of variably altered metabasalt. Preferential orientation of clinopyroxene was observed, likely recording a magmatic fabric.

Vein-like orthopyroxene was observed in serpentinized dunite (interval 4R-1, 50–53 cm). The orthopyroxene veins irregularly cut olivine grains (Figure F10) and likely precipitated from evolved magmas infiltrating dunite well after the formation of dunitic channels (which likely formed during interaction between an early orthopyroxene-undersaturated melt and harzburgite). Veins are severely disturbed by talc-chlorite and serpentine veins.

Section 8R-1 has only one unit of mixed rubble of subrounded to angular pieces of talc-amphibole schist and basalt (fragments up to 6 cm). Basalts vary from fragments with rare amphibole micro-liths at the top of the core to aphyric texture at the bottom.

Alteration

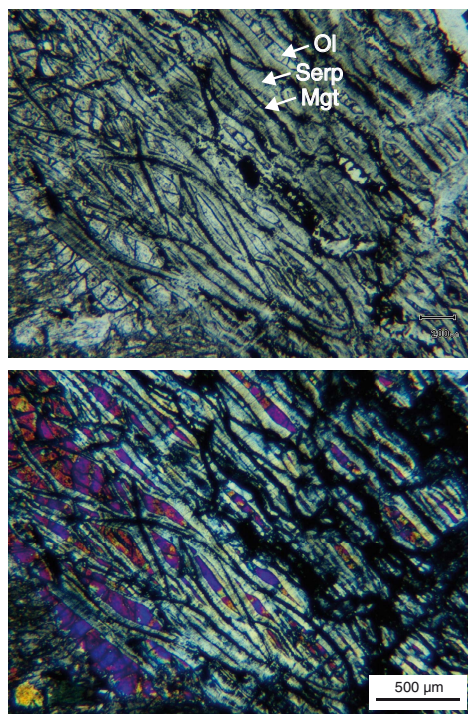
As described above, Site M0068 lithologies comprise a large range of ultramafic and mafic rocks, local melt impregnation, and polymict breccias that contain basaltic clasts at the bottom of Hole M0068B. Four types of alteration were observed: serpentinization, talc-amphibole-chlorite metasomatism, oxidation, and chlorite-amphibole-dominated alteration of gabbros (classified and logged as “other”). Hole M0068A only contains talc-amphibole-chlorite metasomatism, which also dominates the alteration in Hole M0068B. In Hole M0068B, this metasomatism is present throughout the entire hole and is locally associated with additional alteration types. Ser-

pentinization is restricted to four intervals (0–1, 2.48–2.78, 4–5, and 8.90–8.98 mbsf) (Figure F8), and oxidation is only present in the uppermost 5 m. “Other” alteration only occurs in intervals hosting gabbroic lithologies in the uppermost 4 mbsf. Alteration shows a trend of increasing intensities with depth, with all alteration types in cores deeper than 5 mbsf characterized as very high to complete (particularly talc-amphibole-chlorite metasomatism). The least altered intervals are associated with gabbroic lithologies and areas of oxidation. Alteration at Site M0068 is dominated by pervasive alteration (talc-amphibole-chlorite metasomatism and serpentinization) with rare intervals of localized talc-amphibole-chlorite metasomatism or oxidation in Hole M0068B. Alteration of gabbros is present as both pervasive background alteration and alteration patches.

Serpentinization

The four ultramafic intervals recovered in Hole M0068B are variably serpentinized harzburgites and dunites. They are observed in cores with visible bastites and a green to dark green background. The least serpentinized interval occurs in Core 4R and consists of serpentinized metagabbro-impregnated harzburgite. Thin sections from this interval (Samples 4R-1, 18–22 and 50–53 cm) reveal that the serpentinization is preferentially oriented. Corridors of totally serpentinized ribbon mesh texture coat moderately serpentinized olivine (<40% of serpentinization) (Figure F11). Orthopyroxenes are also partially affected by serpentinization. Fibrous, banded, and lamellar to granular serpentine veins crosscut the mesh texture. XRD data confirm the presence of fresh primary minerals, and the serpentine mineralogy is dominated by chrysotile rather than lizardite. XRD samples from additional serpentinized intervals (Samples 1R-1, 38–40 cm, and 2R-1, 83–85 cm) suggest that they are totally serpentinized with a predominance of lizardite and chryso-

Figure F11. Ribbon-shaped mesh texture wrapping around poorly serpentinized olivine (Ol) domains in a serpentinized (Serp) harzburgite (357-M0068B-4R-1, 18–22 cm). Mgt = magnetite.

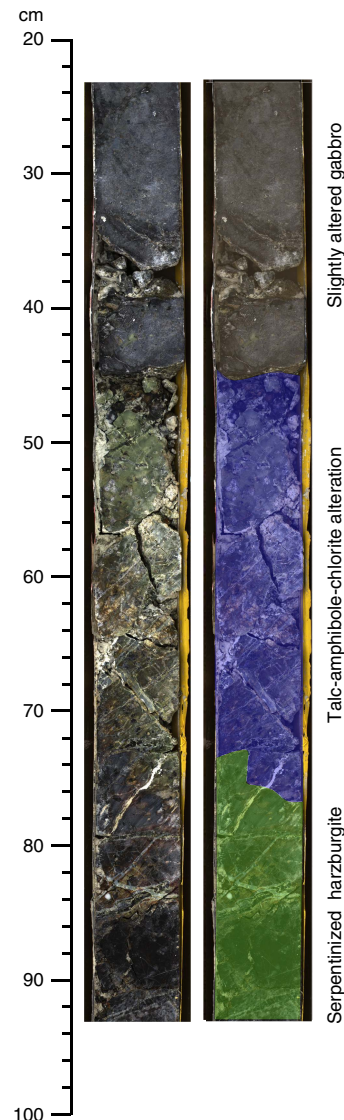


tile, respectively. Texturally, the interval in Core 1R shows areas of macroscopic mesh texture between corridors of sheared talc-amphibole-chlorite assemblages.

Talc-amphibole-chlorite metasomatism

Pervasive alteration to talc-amphibole-chlorite assemblages is present in both Holes M0068A and M0068B. In Hole M0068B, it occurs in three intervals: 1R-1, 90–125 cm, 2R-1, 45–78 cm, and 4R-1, 17–56 cm (Figure F8). In Section 2R-1, it developed as a pale green zone in contact with a slightly altered gabbroic interval and has a gradational transition with the underlying serpentinized harzburgite interval (Figure F12). The presence of relict spinels indicates a metasomatized harzburgitic protolith. Talc, amphibole, and chlorite were identified by XRD measurements (Sample 2R-1, 55–56 cm), and the transition from serpentinized harzburgite is associated with talc, amphibole, and chlorite plus chrysotile (Sample 2R-1, 83–85 cm). Thin section observations (Samples 2R-1, 50–55 and 78–85 cm) show that talc developed by replacement of serpentine after olivine and replacement of bastites by amphibole and chlorite (Figure F12). This zone is crosscut by green talc veins up to 5 mm wide and very dark veins that may be very fine grained gabbroic veins. The top of Core 1R resembles the talc-amphibole-chlorite schist described in Hole M0068A (Sample 1R-1, 34–35 cm) with the addition of serpentine. In both cases, total alteration of primary minerals (plagioclase, pyroxene, and olivine) is confirmed by thin section observation (Samples 357-M0068A-1R-1, 34–35 cm, and 357-M0068B-1R-1, 118.5–121 cm) and XRD measurements (Samples 357-M0068A-1R-1, 34–35 cm, and 357-M0068B-1R-1, 38–40 and 79.5–81 cm), and talc, amphibole, and chlorite were observed. These intervals show evidence for melt intrusion overprinted by variable degrees of metasomatism with an unknown protolith. In

Figure F12. Split core line scan image and annotated sketch (357-M0068B-2R-1) showing gabbro intrusion (0–44 cm) with adjacent talc-chlorite-amphibole metasomatism (44–75 cm) that has a gradational boundary with serpentinized harzburgite (75–92 cm).

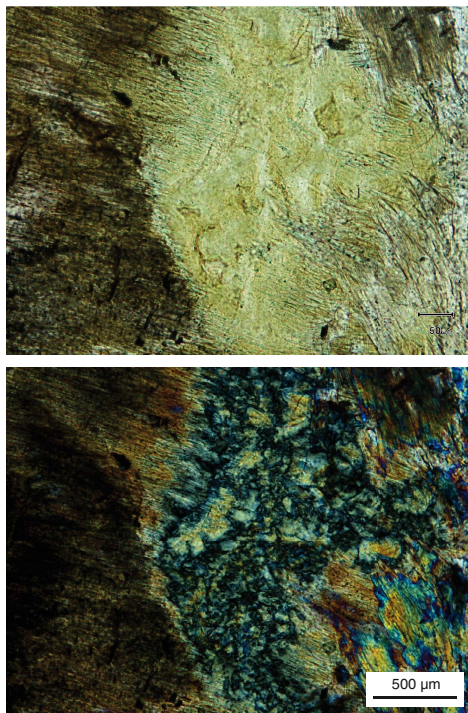


interval 357-M0068B-4R-1, 17–56 cm, partially serpentinized harzburgite was affected by melt impregnation (thin section: Samples 4R-1, 18–22 and 50–53 cm; XRD: Sample 4R-1, 18–21 cm). The partial serpentinization of olivine and pyroxene produced serpentine textures. Gabbroic impregnation formed plagioclase and clinopyroxene-rich zones that are locally altered to chlorite and tremolite.

Other alteration of gabbros

Hole M0068B contains intervals (1R-1, 125–150 cm, and 2R-1, 0–45 cm) of slightly to moderately altered gabbroic rocks that locally preserve primary magmatic textures. Thin section observations (Samples 1R-1, 134–139 cm, and 2R-1, 31–36.5 cm) show replacement of plagioclase and orthopyroxene by chlorite and replacement of clinopyroxene by amphibole (Figure F13), and this mineral assemblage is confirmed by the XRD results. Thin section

Figure F13. Replacement of pyroxene by amphibole and chlorite (357-M0068B-2R-1, 31–36.5 cm).



observations and XRD results differ for Sample 1R-1, 134–139 cm, likely because of the limited size of the XRD sample (2.3 g) compared to the coarse-grained texture of the gabbro.

Oxidation

Oxidation is restricted to the serpentinized intervals above 5 mbsf and is localized as patches close to contacts with talc-amphibole-chlorite-bearing metasomatized intervals or slightly altered gabbroic intrusions.

Veins and crosscutting relationships

Veins are present throughout Hole M0068B, and vein intensity varies between 1–5 and >20 veins per 10 cm (vein intensity scale is 2 to 5) (see Figure F15 in the Expedition 357 methods chapter [Früh-Green et al., 2017b]). Veins are predominantly pale green to white and often occur with a banded internal structure, implying multiple fluids traveled along the same vein. The dominant vein mineralogy is talc, and intervals of high-intensity parallel talc veins with irregular to sigmoidal shape are present (e.g., Figure F14). Relative age relationships are observable in Section 4R-1, with (from oldest to youngest) 0.5–1 mm white (talc) veins, 2 mm green veins, and 1–3 mm white veins. In thin section, quartz-chlorite veins are also present (Sample 8R-1, 15–20 cm). Talc-amphibole-chlorite metasomatized intervals are pervasively altered. In thin section, however, talc veins crosscut the pervasive alteration (Sample 4R-1, 18–22 cm), indicating multiple incursions of silica-rich fluids into the rocks. In thin sections of partially serpentinized harzburgites and dunites, serpentine veins with banded or composite internal structure have cores of either serpentine, chlorite, or talc, indicating that veins were repeatedly exploited by multiple generations of fluids that passed through these rocks.

Figure F14. Series of sigmoidal to irregular isolated talc veins that form a subparallel network (357-M0068B-4R-1, 78–88 cm).



Overprinting relationships and alteration history

Observations in the eastern sites indicate that the initial serpentinization of harzburgite is locally overprinted by talc-amphibole-chlorite metasomatism. Complex vein relationships show these rocks experienced a complex series of hydrothermal interaction with repeated incursions of similar silica-rich fluids.

Mineralogy from XRD data

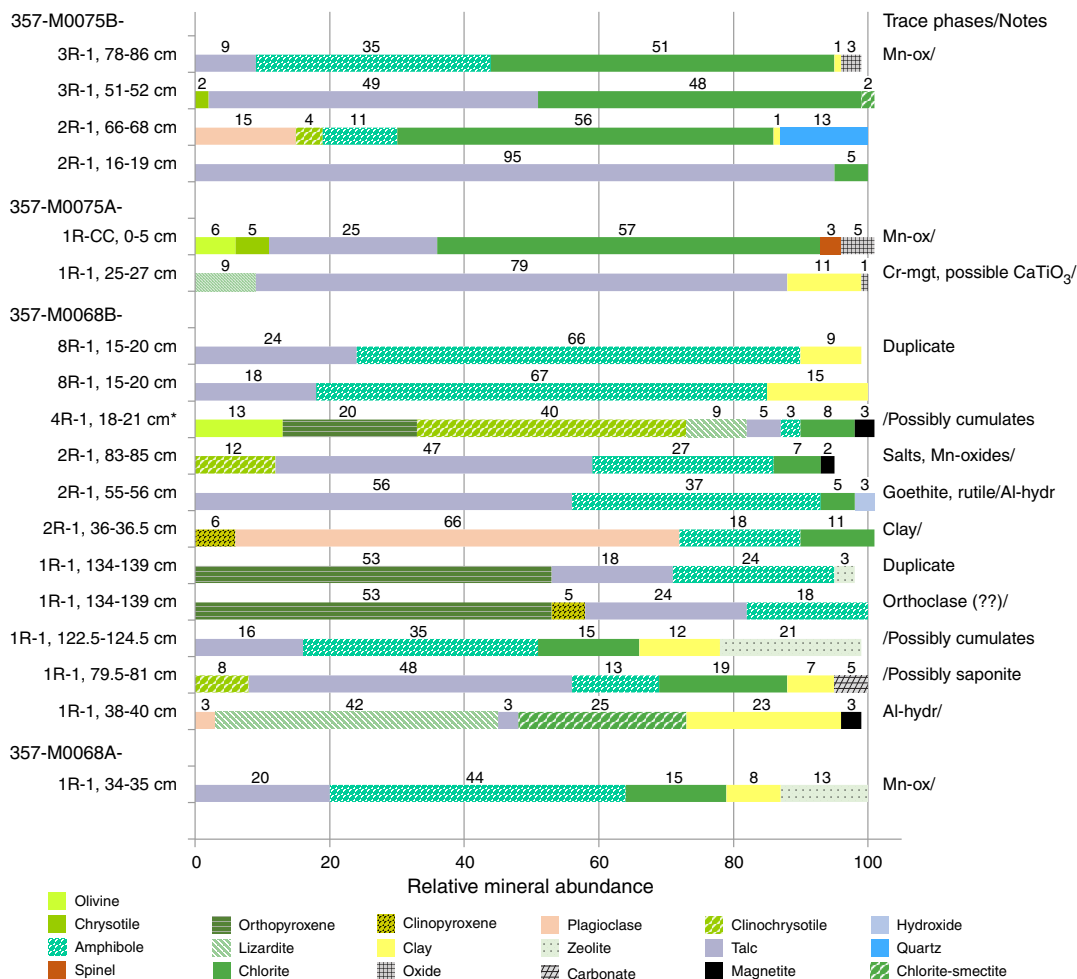
Samples for XRD analysis were taken from the four holes at the two eastern drill sites (Figure F15). The most commonly identified phases were secondary minerals, namely talc, amphibole, and chlorite. Chlorite occurs in greater relative proportion in Site M0075 samples, whereas amphibole was found in greater relative proportion and more frequently in Site M0068 samples. Serpentine including lizardite, chrysotile, and clinochrysotile occurs in significant proportions in only 2 of the 12 Site M0068 samples. Primary phases including olivine, orthopyroxene, and plagioclase were found in only four samples (three from Site M0068) with no specific relationship with depth. Minor phases detected include clays, magnetite, zeolite, Mn oxides (likely derived from seawater interaction), and hydroxides. Quartz was found in a single sample from Site M0075 and is attributed to the existence of a quartz vein observed in thin section. XRD results for each site are provided in Table T2.

Structure

Site M0068 is located over the striated surface of Atlantis Massif, ≈4 km west of Site M0075. High-resolution multibeam bathymetry indicates a fault oriented oblique to the spreading axis, which truncates striations on the fault surface plunging ≈10° toward the axis (Figure F2B). The fault scarp dips away from the Mid-Atlantic Ridge (northwest) and shows ≈10–15 m vertical relief. Holes M0068A and M0068B were drilled on the downdropped block, over the striated surface itself, ≈50 m away from the base of the fault scarp.

Hole M0068A is less than 1 m deep, and Hole M0068B ends at 9.6 mbsf. No structural correlation can be made between the two holes. Hole M0068A is composed of loose rubble varying in size from <1 to >10 cm. Rocks are variably foliated, with deformed talc-rich schistose material and serpentinite clasts. Hole M0068B shows an upper structural interval from 0 to 5.7 mbsf (Sections 1R-1 through 4R-CC) that contains intervals of breccia with cemented matrix and intercalated sections of variably altered peridotite and gabbro (Figure F16) continuous over ≈10 to >100 cm core lengths.

Figure F15. Relative abundance of mineral phases identified by bulk powder XRD analysis, Sites M0075 and M0068. Colors correspond to mineral phases merged as groups (see **Core description** in the Expedition 357 methods chapter for mineral group definitions [Früh-Green et al., 2017b]). Numbers are semi-quantitative abundances determined from fits to XRD peak patterns. Trace phases are subject to large uncertainties. * = poor data quality.



The lower structural interval (Sections 6R-1 through 8R-1) corresponds to loose rubble with clast sizes from <1 to ~10 cm. Section 5R-1 is not in situ and contains drilled rubble that fell into the hole during operations.

Cemented breccia intervals contain angular polymict clasts of variable size. Contacts with other rock types are locally preserved (Figure F16) and show no evidence of deformation. The base of the serpentinite unit in Section 1R-1 is irregularly fractured and cemented to the breccia and does not show any deformation structure. This serpentinite block is also crosscut by a steeply dipping schistose shear zone. Below a fracture that cuts both a piece of serpentinite and the adjacent shear zone, an interval is occupied by breccia cemented to the shear zone. Serpentinite and gabbro show variable veining and fracturing but do not display apparent structural continuity.

The lower structural levels (below 5.8 mbsf; Cores 6R–8R) are composed of loose rubble. Clasts are primarily highly foliated schistose talc schists with associated cataclasis, some with red alteration halos (oxidation), and shattered dolerite (Figure F17). The upper structural level is likely not in situ (rubble and carbonate matrix

breccia), and the structural integrity of the lower level is uncertain (loose rubble with no preserved contacts).

Despite this uncertainty, within particular sections there are important relationships between serpentinitized peridotite, gabbroic veins, and talc-tremolite-chlorite alteration. For example, in interval 1R-1, 15–31 cm, several zones of low-strain cataclasis and shearing are present, with talc and tremolite partially replacing serpentinite and talc growing in vein walls. These zones may reveal insights about the interaction between deformation and metasomatic alteration. Other zones, such as the steep shear zone shown in Figure F16, appear to have a largely metabasic protolith and may have nucleated on gabbroic veins.

Thin section observations of cored intervals recovered from Site M0068 (gabbro and peridotite) reveal a limited high-temperature strain history restricted to millimetric shear zones hosting weak crystal-plastic deformation. Lower temperature deformation appears to be focused into metagabbroic intervals in peridotite, with tremolite showing evidence of dynamic recrystallization and often being affected by cataclasis (Figure F18). Serpentinized harzburgite shows little signs of deformation, with talc alteration generally post-tectonic within the sampled intervals.

Table T2. X-ray diffraction results, Holes M0068A, M0068B, M0075A, and M0075B. * = poor data quality, † = duplicate sample. Percentages were released by the software, sometimes with excess. Total sum <100% likely reflects the presence of amorphous or poorly crystallized material. [Download table in .csv format.](#)

| Core, section, interval (cm) | All minerals present (proportion) |
|------------------------------|--|
| 357-M0068A-1R-1, 34–35 | Amphibole (44), talc (20) chlorite (15), clay (8), zeolite (13) |
| 357-M0068B-1R-1, 38–40 | Plagioclase (3), lizardite (42), talc (3), chlorite-smectite (25), clay (23), magnetite (3) |
| 1R-1, 79.5–81 | Clino-chrysotile (8), talc (48), amphibole (13), chlorite (19), clay (7), carbonates (5) |
| 1R-1, 122.5–124.5 | Talc (16), amphibole (35), chlorite (15), clay (12), zeolite (21) |
| 1R-1, 134–139 | Orthopyroxene (53), clinopyroxene (5), talc (24), amphibole (18) |
| 1R-1, 134–139† | Orthopyroxene (53), talc (18), amphibole (24), zeolite (3) |
| 2R-1, 36–36.5 | Clinopyroxene (6), plagioclase (66), amphibole (18), chlorite (11) |
| 2R-1, 55–56 | Talc (56), amphibole (37), chlorite (5), hydroxides (3) |
| 2R-1, 83–85 | Clino-chrysotile (12), talc (47), amphibole (27), chlorite (7), magnetite (2) |
| 4R-1, 18–21* | Olivine (13), orthopyroxene (20), clino-chrysotile (40), lizardite (9), talc (5), amphibole (3), chlorite (8), magnetite (3) |
| 8R-1, 15–20 | Talc (18), amphibole (67), clay (15) |
| 8R-1, 15–20† | Talc (24), amphibole (66), clay (9) |
| 357-M0075A-1R-1, 25–27 | Lizardite (9), talc (79), clay (11), oxides (1) |
| 1R-CC, 0–5 | Olivine (6), chrysotile (5), talc (25), chlorite (57), spinel (3), oxides (5) |
| 357-M0075B-2R-1, 16–19 | Talc (95), chlorite (5) |
| 2R-1, 66–68 | Plagioclase (15), clino-chrysotile (4), amphibole (11), chlorite (56), clay (1), quartz (13) |
| 3R-1, 51–52 | Chrysotile (2), talc (49), chlorite (48), chlorite-smectite (2) |
| 3R-1, 78–86 | Talc (9), amphibole (35), chlorite (51), clay (1), oxides (3) |

Figure F16. Cemented breccia in contact with serpentinized peridotite both at its base and along a schistose deformation zone (357-M0068A-1R-1, 50–74 cm).



Figure F17. A. Fault breccia comprising foliated fault schist clasts (357-M0068B-8R-1, 15–20 cm; PPL). Breccia is cut by a later quartz-chlorite vein (lower left corner). B. Well-developed schistose fabric in one tremolite-rich clast hosted in the breccia (XPL). C. Large tremolite grain in another clast broken up into a thin zone of cataclasis (XPL).

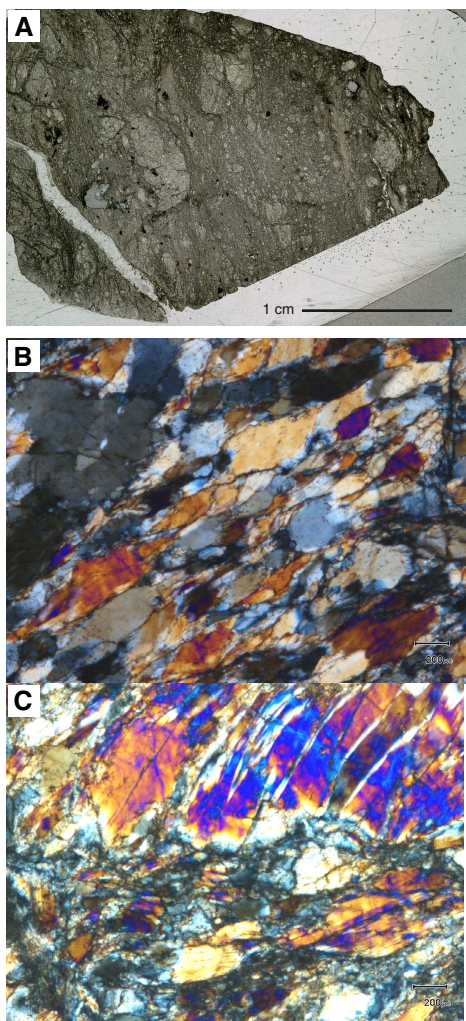
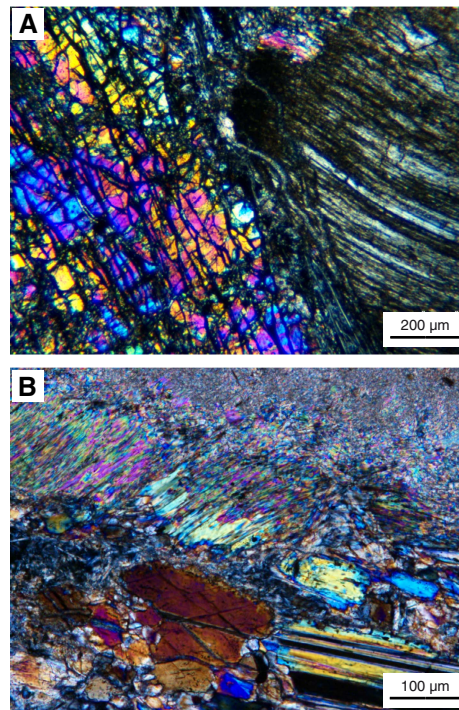


Figure F18. A. Olivine with tight and well-oriented microfractures and incipient recrystallization (357-M0068B-4R-1, 18–22 cm; XPL). Note curved cleavage in orthopyroxene porphyroclasts. These microstructures are characteristic of those formed during semibrittle deformation at Site M0068. B. Aligned and partially recrystallized amphibole overprinted by talc (1R-1, 34–35 cm; XPL). Amphiboles have prismatic or euhedral shapes and are preferentially aligned, defining a foliation. Undeformed talc has grown from former serpentine clasts toward the amphibole-rich zone.



Bulk rock geochemistry

Bulk carbon analyses

Ten samples were collected shipboard for bulk rock carbon analysis and analyzed during the Onshore Science Party (OSP) for total carbon (TC), total inorganic carbon (TIC), and total organic carbon (TOC). These standard shipboard samples were not collected in a manner to avoid external carbon contamination (see [Geochemistry](#) in the Expedition 357 methods chapter [Früh-Green et al., 2017b]); therefore, values should be viewed with extreme caution and considered maximum concentrations. All samples were run in a single batch against the same standards, and all data are presented in one table (Table T3). TC for shipboard samples ranges from <0.05 to <0.96 wt% with a coefficient of variance of the measurements generally above 20%. TOC measured in shipboard samples ranges from 0.04 to 0.09 wt%, resulting in TIC (by subtraction of TOC from TC) estimates of 0 to 0.87 wt%.

Whole-rock major and trace elements

After the OSP, whole-rock major and trace element analyses were carried out on representative shipboard samples ($N = 19$) at the Pacific Centre for Isotopic and Geochemical Research at the University of British Columbia, Canada (see [Geochemistry](#) in the Expedition 357 methods chapter [Früh-Green et al., 2017b]). Samples were selected at sea and during the OSP to represent the various key lithologies present in the drill cores. All whole-rock

Table T3. TC, TIC, and TOC content in standard shipboard samples, Sites M0068, M0069, M0071, M0072, M0075, and M0076. [Download table in .csv format.](#)

Table T4. Chemical compositions of representative lithologies, Sites M0068, M0069, M0071, M0072, M0075, and M0076. Major elements were measured by ICP-OES, and trace elements were measured by high-resolution inductively coupled plasma-mass spectrometry (HR-ICP-MS) using a Thermo Finnigan Element2 ICP-MS. LOI = loss on Ignition. $Mg\# = Mg/(Mg + Fe) \times 100$. (Continued on next page.) [Download table in .csv format.](#)

| Hole, core, section, interval (cm) | Top depth (mbsf) | Bottom depth (mbsf) | Lithology | SiO ₂ (wt%) | TiO ₂ (wt%) | Al ₂ O ₃ (wt%) | Fe ₂ O ₃ (wt%) | MnO (wt%) | MgO (wt%) | CaO (wt%) | Na ₂ O (wt%) | K ₂ O (wt%) | P ₂ O ₅ (wt%) | Total (wt%) | LOI (wt%) | Mg# |
|------------------------------------|------------------|---------------------|---|------------------------|------------------------|--------------------------------------|--------------------------------------|-----------|-----------|-----------|-------------------------|------------------------|-------------------------------------|-------------|-----------|-----|
| Eastern sites | | | | | | | | | | | | | | | | |
| M0068A-1R-1, 34–35 | 0.340 | 0.350 | Talc-amphibole-chlorite schist | 50.01 | 0.10 | 4.27 | 8.49 | 0.14 | 22.87 | 2.64 | 0.26 | 0.00 | 0.04 | 88.82 | 5.34 | 70 |
| M0068B-1R-1, 37.5–40 | 0.375 | 0.400 | Serpentinized peridotite | 40.03 | 0.03 | 1.16 | 9.98 | 0.11 | 38.78 | 0.25 | 0.15 | 0.05 | 0.00 | 90.52 | 11.95 | 77 |
| M0068B-1R-1, 134–139 | 1.340 | 1.390 | Gabbro | 52.14 | 0.43 | 16.40 | 8.30 | 0.15 | 9.25 | 11.62 | 2.82 | 0.00 | 0.04 | 101.16 | 0.41 | 49 |
| M0068B-2R-1, 31–36 | 2.030 | 2.080 | Gabbro | 50.77 | 0.30 | 17.53 | 6.75 | 0.13 | 8.98 | 11.27 | 2.75 | 0.00 | 0.01 | 98.50 | 0.30 | 53 |
| M0068B-2R-1, 52–55 | 2.240 | 2.270 | Talc-amphibole-chlorite schist | 59.63 | 0.02 | 1.05 | 6.68 | 0.14 | 28.14 | 1.66 | 0.22 | 0.02 | 0.01 | 97.56 | 4.30 | 78 |
| M0075B-2R-1, 66–68 | 2.940 | 2.960 | Metadolerite | 47.09 | 1.08 | 18.23 | 12.09 | 0.12 | 11.23 | 7.90 | 1.88 | 0.00 | 0.07 | 99.69 | 3.33 | 44 |
| Central sites | | | | | | | | | | | | | | | | |
| M0069A-5R-1, 29.5–32 | 7.175 | 7.200 | Metadolerite | 26.31 | 0.92 | 18.48 | 27.46 | 0.17 | 16.68 | 1.06 | 0.14 | 0.00 | 0.06 | 91.28 | 8.31 | 34 |
| M0069A-5R-1, 110–113 | 7.980 | 8.010 | Metadolerite | 31.61 | 1.40 | 20.36 | 18.75 | 0.16 | 17.41 | 3.58 | 0.66 | 0.02 | 0.12 | 94.06 | 7.86 | 44 |
| M0069A-10R-1, 80–87 | 15.520 | 15.590 | Serpentinized harzburgite | 36.19 | 0.03 | 1.02 | 8.85 | 0.08 | 37.71 | 1.75 | 0.09 | 0.00 | 0.00 | 85.71 | 13.58 | 79 |
| M0069A-10R-3, 0–2.5 | 16.290 | 16.315 | Serpentinized dunite | 33.08 | 0.03 | 1.58 | 10.98 | 0.07 | 39.22 | 0.18 | 0.00 | 0.00 | 0.01 | 85.14 | 13.81 | 75 |
| M0072B-5R-1, 37–38 | 6.355 | 6.365 | Talc-amphibole-chlorite schist | 50.64 | 0.14 | 3.82 | 3.35 | 0.06 | 26.06 | 7.66 | 0.21 | 0.00 | 0.02 | 91.97 | 4.73 | 87 |
| M0072B-7R-1, 72.5–75 | 9.713 | 9.738 | Impregnated/metasomatized serpentinized harzburgite | 42.41 | 0.03 | 1.05 | 9.79 | 0.09 | 37.03 | 0.72 | 0.15 | 0.00 | 0.01 | 91.28 | 10.82 | 76 |
| M0072B-8R-1, 34–38 | 11.048 | 11.088 | Impregnated/metasomatized serpentinized harzburgite | 38.60 | 0.03 | 1.22 | 9.91 | 0.09 | 37.61 | 0.45 | 0.09 | 0.00 | 0.00 | 88.00 | 12.38 | 76 |
| M0072B-8R-2, 76–77 | 12.268 | 12.278 | Impregnated/metasomatized serpentinized harzburgite | 43.53 | 0.05 | 1.86 | 6.92 | 0.13 | 33.18 | 2.26 | 0.35 | 0.00 | 0.01 | 88.28 | 10.27 | 80 |
| M0076B-7R-1, 81–83 | 10.534 | 10.554 | Serpentinized harzburgite | 39.55 | 0.03 | 0.86 | 8.24 | 0.20 | 37.86 | 1.03 | 0.14 | 0.01 | 0.02 | 87.94 | 12.97 | 80 |
| Western sites | | | | | | | | | | | | | | | | |
| M0071A-1R-2, 120–121 | 1.780 | 1.790 | Serpentinized dunite | 36.62 | 0.02 | 1.11 | 9.06 | 0.08 | 40.05 | 0.09 | 0.00 | 0.00 | 0.01 | 87.04 | 12.10 | 79 |
| M0071A-2R-1, 64–67 | 3.360 | 3.390 | Metagabbro | 26.21 | 0.24 | 21.04 | 32.07 | 0.68 | 14.19 | 0.40 | 0.28 | 0.03 | 0.02 | 95.14 | 8.49 | 26 |
| M0071C-1R-1, 11–13 | 0.110 | 0.130 | Serpentinized harzburgite | 37.75 | 0.02 | 1.17 | 9.19 | 0.11 | 39.58 | 0.10 | 0.00 | 0.00 | 0.02 | 87.94 | 11.82 | 79 |
| M0071C-2R-1, 74–76 | 3.420 | 3.440 | Serpentinized harzburgite | 39.95 | 0.05 | 1.27 | 9.34 | 0.10 | 39.49 | 0.27 | 0.10 | 0.05 | 0.02 | 90.64 | 12.06 | 78 |
| | | | Maximum: | 59.63 | 1.40 | 21.04 | 32.07 | 0.68 | 40.05 | 11.62 | 2.82 | 0.05 | 0.12 | 101.16 | 13.81 | 87 |
| | | | Minimum: | 26.21 | 0.02 | 0.86 | 3.35 | 0.06 | 8.98 | 0.09 | 0.00 | 0.00 | 0.00 | 85.14 | 0.30 | 26 |

geochemical data for the expedition are reported in common tables because all measurements were made under the same analytical conditions using a common set of standards. Major element concentrations are described in the text as weight percent oxides calculated from raw elemental values (Table T4) and are reported as volatile-free concentrations normalized to 100% in Table T5. Magnesium numbers ($Mg\#$) were calculated as molar ($Mg/[Mg + Fe] \times 100$) (Figure F19). Trace element data for each area are given in Table T4. Trace element data from the eastern sites are plotted in two sets of figures: as rare earth element (REE) diagrams normalized to chondrite (Figure F20) and as extended trace element plots normalized to primitive mantle (PM) (Figure F21).

Summary of all sites

The compositional ranges in major and trace elements measured in the 19 bulk rock samples reflect lithology differences as well as the type and intensity of alteration (Tables T4, T5). The sum of measured major elements varies from 85.7 to 101.2 wt% due to heterogeneous degrees of alteration and water incorporation. Trace element abundances are generally in the parts to subparts per million range, with the exception of high Ni and Cr concentrations in the ultramafic lithologies.

Independently of the site location, altered ultramafic lithologies and talc-amphibole-chlorite schists form two groups within the SiO₂-MgO space (Table T5; Figure F22). Talc-amphibole-chlorite schists are associated with the highest SiO₂/MgO ratios ($SiO_2 > 55.1$ wt% [normalized concentrations] and $MgO < 28.9$ wt%), whereas serpentinized ultramafic lithologies are associated with the lowest ratios ($SiO_2 < 49.3$ and $MgO > 37.6$ wt%). A trend is identifiable

Table T4 (continued).

| Hole, core, section, interval (cm) | Cr (ppm) | Ni (ppm) | Li (ppm) | Sc (ppm) | V (ppm) | Co (ppm) | Cu (ppm) | Zn (ppm) | Ga (ppm) | Rb (ppm) | Sr (ppm) | Y (ppm) | Zr (ppm) | Nb (ppm) | Mo (ppm) | Cd (ppm) | Sn (ppm) | Sb (ppm) | Cs (ppm) |
|------------------------------------|----------|----------|----------|----------|---------|----------|----------|----------|----------|----------|----------|---------|----------|----------|----------|----------|----------|----------|----------|
| Eastern sites | | | | | | | | | | | | | | | | | | | |
| M0068A-1R-1, 34–35 | 1,349 | 1,640 | 13.12 | 7.91 | 28.9 | 77.8 | 17.81 | 73.3 | 7.34 | 0.11 | 3.96 | 41.57 | 5.43 | 1.89 | 0.46 | 29.4 | 1.28 | 0.05 | 0.00 |
| M0068B-1R-1, 37.5–40 | 3,079 | 1,651 | 6.29 | 10.37 | 41.6 | 95.0 | 24.24 | 56.9 | 1.21 | 0.13 | 3.29 | 1.03 | 0.33 | 0.06 | 0.40 | 27.5 | 0.82 | 0.29 | 0.00 |
| M0068B-1R-1, 134–139 | 100 | 97 | 5.65 | 41.62 | 190 | 37.8 | 48.95 | 48.4 | 14.86 | 0.36 | 82.0 | 14.84 | 17.45 | 0.30 | 0.16 | 62.1 | 1.16 | 0.03 | 0.01 |
| M0068B-2R-1, 31–36 | 142 | 94 | 4.39 | 35.61 | 151 | 35.1 | 44.11 | 38.7 | 14.46 | 0.16 | 85.0 | 8.08 | 4.76 | 0.05 | 0.20 | 35.4 | 0.26 | 0.02 | 0.01 |
| M0068B-2R-1, 52–55 | 1,746 | 1,741 | 21.67 | 7.56 | 18.6 | 56.2 | 18.39 | 86.7 | 2.03 | 0.11 | 2.36 | 0.43 | 0.41 | 0.05 | 0.15 | 9.3 | 0.37 | 0.03 | 0.00 |
| M0075B-2R-1, 66–68 | 414 | 226 | 12.48 | 35.90 | 179 | 53.3 | 1.56 | 24.0 | 17.29 | 0.27 | 72.5 | 27.57 | 39.78 | 1.24 | 0.18 | 20.2 | 0.83 | 0.01 | 0.01 |
| Central sites | | | | | | | | | | | | | | | | | | | |
| M0069A-5R-1, 29.5–32 | 680 | 341 | 6.76 | 37.40 | 198 | 191 | 0.04 | 43.6 | 18.54 | 0.07 | 1.73 | 22.71 | 23.45 | 0.35 | 0.21 | 8.6 | 0.55 | 0.01 | 0.00 |
| M0069A-5R-1, 110–113 | 523 | 436 | 12.76 | 41.16 | 292 | 149 | 0.58 | 38.3 | 23.42 | 0.13 | 58.0 | 31.68 | 20.82 | 1.56 | 0.14 | 16.6 | 0.81 | 0.00 | 0.01 |
| M0069A-10R-1, 80–87 | 8,363 | 6,531 | 2.59 | 29.24 | 84.7 | 282 | 4.82 | 88.1 | 2.96 | 0.00 | 758 | 2.18 | 1.23 | 0.05 | 0.62 | 17.5 | 0.20 | 0.01 | 0.00 |
| M0069A-10R-3, 0–2.5 | 29,698 | 7,931 | 0.22 | 14.31 | 116 | 408 | 14.42 | 255 | 7.10 | 0.00 | 3.61 | 0.09 | 0.00 | 0.05 | 0.37 | 15.5 | 0.14 | 0.01 | 0.00 |
| M0072B-5R-1, 37–38 | 1,986 | 1,253 | 0.15 | 17.68 | 59.8 | 33.1 | 3.34 | 6.7 | 5.56 | 0.00 | 2.72 | 7.15 | 4.11 | 0.15 | 0.01 | 4.1 | 0.22 | 0.00 | 0.00 |
| M0072B-7R-1, 72.5–75 | 2,746 | 3,687 | 1.47 | 9.71 | 28.1 | 155 | 0.76 | 21.3 | 2.13 | 0.10 | 2.13 | 3.54 | 1.54 | 0.49 | 0.21 | 6.8 | 0.23 | 0.00 | 0.01 |
| M0072B-8R-1, 34–38 | 3,614 | 2,193 | 0.49 | 6.60 | 25.6 | 101 | 0.17 | 21.2 | 1.74 | 0.05 | 1.02 | 1.84 | 1.17 | 0.47 | 0.18 | 6.4 | 0.28 | 0.00 | 0.00 |
| M0072B-8R-2, 76–77 | 2,663 | 1,984 | 1.94 | 8.35 | 32.1 | 76.8 | 1.41 | 15.6 | 3.17 | 0.31 | 3.01 | 7.12 | 5.11 | 0.51 | 0.21 | 10.0 | 0.53 | 0.02 | 0.02 |
| M0076B-7R-1, 81–83 | 2,420 | 2,810 | 8.73 | 7.95 | 33.7 | 116 | 3.85 | 24.3 | 1.23 | 0.07 | 13.60 | 2.12 | 0.38 | 0.03 | 1.30 | 49.1 | 0.10 | 0.13 | 0.00 |
| Western sites | | | | | | | | | | | | | | | | | | | |
| M0071A-1R-2, 120–121 | 21,572 | 14,590 | 22.74 | 82.79 | 340 | 622 | 120 | 318 | 9.62 | 0.20 | 17.24 | 2.33 | 0.00 | 0.11 | 2.18 | 95.2 | 0.05 | 1.09 | 0.00 |
| M0071A-2R-1, 64–67 | 748 | 190 | 16.60 | 41.08 | 139 | 152 | 0.09 | 331 | 10.49 | 0.16 | 3.01 | 6.88 | 3.13 | 0.02 | 0.22 | 40.9 | 1.71 | 0.02 | 0.01 |
| M0071C-1R-1, 11–13 | 11,705 | 6,715 | 12.95 | 30.04 | 190 | 315 | 231 | 395 | 5.55 | 0.10 | 10.09 | 0.99 | 0.00 | 0.02 | 1.04 | 34.0 | 0.20 | 1.34 | 0.00 |
| M0071C-2R-1, 74–76 | 3,796 | 2,987 | 3.93 | 16.53 | 74.3 | 137 | 15.86 | 64.3 | 1.58 | 0.03 | 3.06 | 0.38 | 0.09 | 0.02 | 0.27 | 26.7 | 0.08 | 0.15 | 0.00 |
| Maximum: | 29,698 | 14,590 | 22.74 | 82.79 | 340 | 622 | 231 | 395 | 23.42 | 0.36 | 758 | 41.57 | 39.78 | 1.89 | 2.18 | 95.2 | 1.71 | 1.34 | 0.02 |
| Minimum: | 100 | 94 | 0.15 | 6.60 | 18.6 | 33.1 | 0.04 | 6.7 | 1.21 | 0.00 | 1.02 | 0.38 | 0.00 | 0.02 | 0.01 | 4.1 | 0.05 | 0.00 | 0.00 |

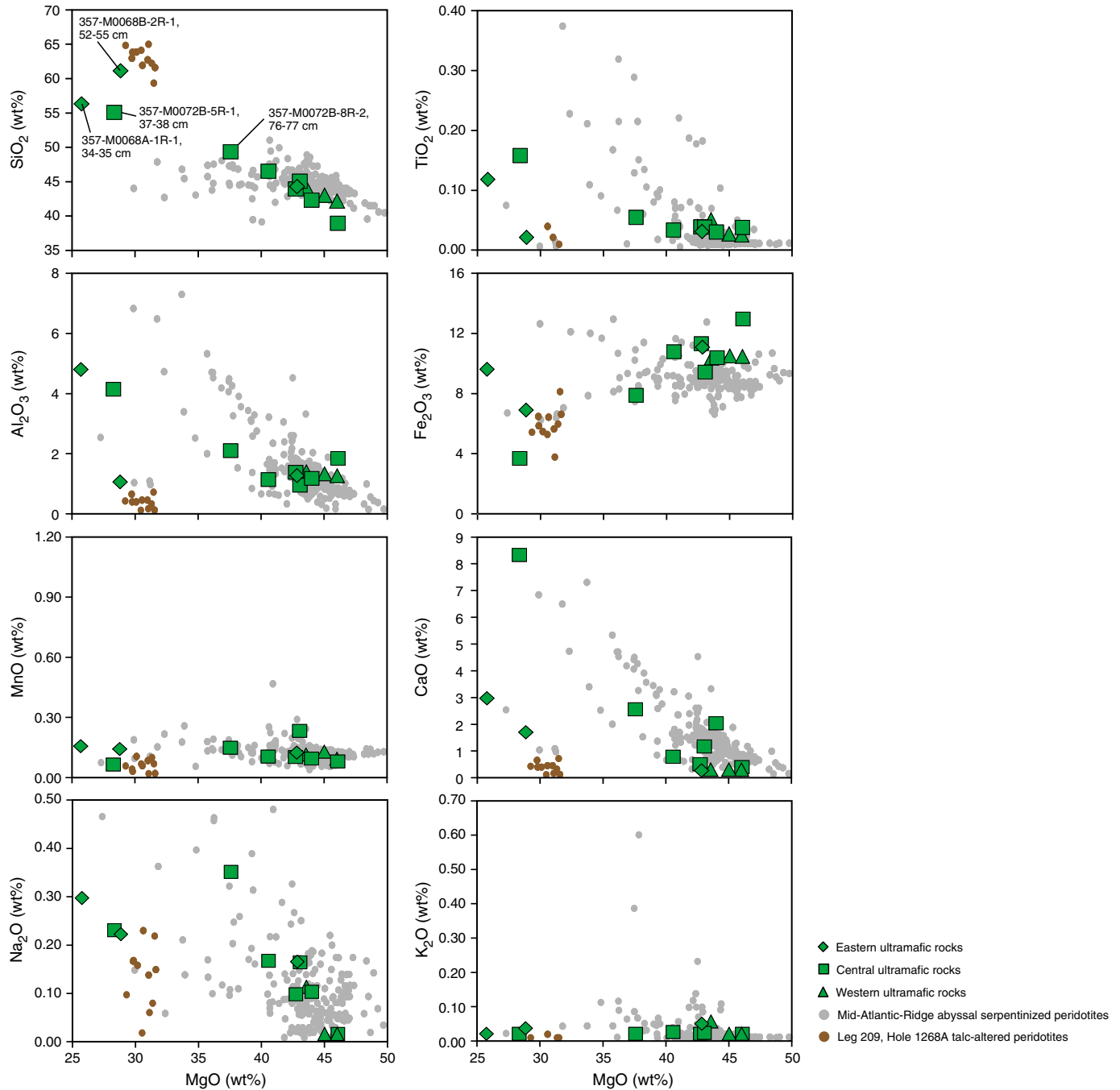
| Hole, core, section, interval (cm) | Ba (ppm) | La (ppm) | Ce (ppm) | Pr (ppm) | Nd (ppm) | Sm (ppm) | Eu (ppm) | Gd (ppm) | Tb (ppm) | Dy (ppm) | Ho (ppm) | Er (ppm) | Tm (ppm) | Yb (ppm) | Lu (ppm) | Hf (ppm) | Ta (ppm) | W (ppm) | Pb (ppm) | Th (ppm) | U (ppm) |
|------------------------------------|----------|----------|----------|----------|----------|----------|----------|----------|----------|----------|----------|----------|----------|----------|----------|----------|----------|---------|----------|----------|---------|
| 357- | | | | | | | | | | | | | | | | | | | | | |
| Eastern sites | | | | | | | | | | | | | | | | | | | | | |
| M0068A-1-1, 34–35 | 0.87 | 8.56 | 30.19 | 3.64 | 16.89 | 4.43 | 0.52 | 4.86 | 0.91 | 5.86 | 1.29 | 4.11 | 0.65 | 4.29 | 0.65 | 0.38 | 0.18 | 0.07 | 0.35 | 0.75 | 0.09 |
| M0068B-1-1, 37.5–40 | 0.88 | 0.30 | 1.32 | 0.14 | 0.61 | 0.16 | 0.25 | 0.17 | 0.03 | 0.21 | 0.05 | 0.16 | 0.03 | 0.18 | 0.03 | 0.02 | 0.01 | 0.05 | 0.25 | 0.03 | 0.47 |
| M0068B-1-1, 134–139 | 4.41 | 0.92 | 3.29 | 0.55 | 3.21 | 1.28 | 0.63 | 1.72 | 0.37 | 2.52 | 0.55 | 1.68 | 0.26 | 1.59 | 0.24 | 0.69 | 0.02 | 1.05 | 0.40 | 0.05 | 0.04 |
| M0068B-2-1, 31–36 | 2.15 | 0.26 | 0.84 | 0.16 | 1.15 | 0.58 | 0.45 | 0.86 | 0.20 | 1.40 | 0.32 | 1.02 | 0.15 | 0.98 | 0.15 | 0.24 | 0.00 | 0.16 | 0.13 | 0.01 | 0.01 |
| M0068B-2-1, 52–55 | 0.23 | 0.09 | 0.28 | 0.03 | 0.15 | 0.04 | 0.04 | 0.05 | 0.01 | 0.07 | 0.02 | 0.06 | 0.01 | 0.07 | 0.01 | 0.01 | 0.00 | 0.11 | 0.17 | 0.01 | 0.06 |
| M0075B-2-1, 66–68 | 2.32 | 1.55 | 5.82 | 1.04 | 6.44 | 2.53 | 0.95 | 3.23 | 0.68 | 4.63 | 0.99 | 2.93 | 0.44 | 2.68 | 0.40 | 1.48 | 0.09 | 0.24 | 0.00 | 0.05 | 0.02 |
| Central sites | | | | | | | | | | | | | | | | | | | | | |
| M0069A-5-1, 29.5–32 | 0.20 | 0.85 | 2.69 | 0.55 | 3.81 | 1.92 | 0.24 | 2.57 | 0.57 | 3.85 | 0.82 | 2.44 | 0.35 | 2.14 | 0.28 | 0.86 | 0.03 | 0.06 | 0.04 | 0.02 | 0.02 |
| M0069A-5-1, 110–113 | 1.33 | 3.05 | 10.48 | 1.59 | 9.26 | 3.33 | 0.96 | 4.09 | 0.80 | 5.13 | 1.08 | 3.17 | 0.45 | 2.76 | 0.40 | 0.87 | 0.10 | 0.04 | 0.09 | 0.06 | 0.06 |
| M0069A-10-1, 80–87 | 0.72 | 0.23 | 0.74 | 0.11 | 0.60 | 0.17 | 0.11 | 0.23 | 0.05 | 0.35 | 0.08 | 0.25 | 0.04 | 0.29 | 0.05 | 0.03 | 0.01 | 0.07 | 0.12 | 0.01 | 2.22 |
| M0069A-10-3, 0–2.5 | 0.00 | 0.00 | 0.02 | 0.00 | 0.03 | 0.01 | 0.01 | 0.00 | 0.00 | 0.00 | 0.00 | 0.00 | 0.00 | 0.02 | 0.01 | 0.00 | 0.00 | 0.03 | 0.22 | 0.00 | 4.50 |
| M0072B-5-1, 37–38 | 0.00 | 0.21 | 1.06 | 0.23 | 1.56 | 0.68 | 0.26 | 0.89 | 0.20 | 1.33 | 0.29 | 0.86 | 0.13 | 0.81 | 0.12 | 0.19 | 0.01 | 0.10 | 0.09 | 0.01 | 0.02 |
| M0072B-7-1, 72.5–75 | 0.00 | 0.47 | 1.72 | 0.25 | 1.23 | 0.34 | 0.10 | 0.40 | 0.08 | 0.52 | 0.12 | 0.39 | 0.07 | 0.47 | 0.08 | 0.10 | 0.03 | 0.10 | 0.09 | 0.09 | 0.16 |
| M0072B-8-1, 34–38 | 0.15 | 0.24 | 0.90 | 0.14 | 0.75 | 0.22 | 0.06 | 0.24 | 0.05 | 0.31 | 0.07 | 0.25 | 0.04 | 0.30 | 0.05 | 0.08 | 0.05 | 0.01 | 0.05 | 0.09 | 0.03 |
| M0072B-8-2, 76–77 | 0.16 | 0.57 | 2.33 | 0.40 | 2.20 | 0.72 | 0.19 | 0.85 | 0.17 | 1.17 | 0.27 | 0.85 | 0.15 | 0.97 | 0.16 | 0.29 | 0.04 | 0.02 | 0.19 | 0.09 | 1.19 |
| M0076B-7-1, 81–83 | 4.58 | 0.13 | 0.29 | 0.08 | 0.49 | 0.15 | 0.07 | 0.20 | 0.04 | 0.27 | 0.07 | 0.20 | 0.03 | 0.21 | 0.03 | 0.01 | 0.01 | 0.08 | 0.07 | 0.00 | 1.98 |
| Western sites | | | | | | | | | | | | | | | | | | | | | |
| M0071A-1-2, 120–121 | 1.19 | 0.16 | 0.33 | 0.06 | 0.40 | 0.17 | 0.10 | 0.33 | 0.05 | 0.36 | 0.09 | 0.29 | 0.06 | 0.46 | 0.09 | 0.00 | 0.00 | 7.62 | 1.91 | 0.00 | 5.05 |
| M0071A-2-1, 64–67 | 0.17 | 0.30 | 0.72 | 0.14 | 1.05 | 0.54 | 0.41 | 0.80 | 0.18 | 1.26 | 0.28 | 0.82 | 0.12 | 0.72 | 0.11 | 0.19 | 0.00 | 0.01 | 0.13 | 0.00 | 0.01 |
| M0071C-1-1, 11–13 | 0.97 | 0.18 | 0.05 | 0.04 | 0.22 | 0.05 | 0.05 | 0.08 | 0.02 | 0.15 | 0.04 | 0.15 | 0.02 | 0.18 | 0.04 | 0.00 | 0.00 | 0.34 | 0.51 | 0.00 | 3.27 |
| M0071C-2-1, 74–76 | 0.30 | 0.00 | 0.00 | 0.00 | 0.01 | 0.00 | 0.02 | 0.00 | 0.00 | 0.03 | 0.01 | 0.04 | 0.01 | 0.07 | 0.02 | 0.00 | 0.01 | 0.02 | 0.57 | 0.00 | 1.52 |
| Maximum: | 4.58 | 8.56 | 30.19 | 3.64 | 16.89 | 4.43 | 0.96 | 4.86 | 0.91 | 5.86 | 1.29 | 4.11 | 0.65 | 4.29 | 0.65 | 1.48 | 0.18 | 7.62 | 1.91 | 0.75 | 5.05 |
| Minimum: | 0.00 | 0.00 | 0.00 | 0.00 | 0.01 | 0.00 | 0.02 | 0.00 | 0.00 | 0.00 | 0.00 | 0.00 | 0.00 | 0.02 | 0.01 | 0.00 | 0.00 | 0.01 | 0.00 | 0.00 | 0.01 |

Table T5. Normalized, volatile-free major element concentrations of representative lithologies, Sites M0068, M0069, M0071, M0072, M0075, and M0076. [Download table in .csv format.](#)

within this second group, with impregnated/metasomatized samples exhibiting the highest SiO₂/MgO ratios and serpentinized dunites the lowest. This trend reflects, on one hand, the crystallization of talc and presence of pyroxenes and, on the other hand, the lack of pyroxenes. Overall, talc-amphibole-chlorite schists (and to a certain extent impregnated/metasomatized ultramafic rocks) appear richer

in Al₂O₃, Na₂O, CaO, and TiO and depleted in Fe₂O₃. Samples from Hole M0068B exhibit the highest SiO₂, CaO, and Na₂O contents and the lowest Al₂O₃ and FeO contents. Mafic samples (gabbros and dolerite) are also divided into two groups (Table T5; Figure F23). In this case, the division relates to the degree of hydration and type of alteration (loss on ignition [LOI] of 0.4, 0.3, and 3.3 wt% for Site

Figure F22. Whole-rock major elements (normalized, volatile-free, and in oxides) vs. MgO for (impregnated/metasomatized) serpentinized ultramafic rocks and talc-amphibole-chlorite schists from Atlantis Massif. Data from Mid-Atlantic-Ridge abyssal serpentinized peridotites and talc-altered peridotites are presented for comparison. Global abyssal peridotite field defined by data from PetDB (<http://www.earthchem.org/petdb>, May 2016). Data for talc-altered peridotite field from Ocean Drilling Program Leg 209, Hole 1268A (also at PetDB).



element (LILE) mobility, but most have significant positive U anomalies.

Site M0075

This shallow site was drilled closest to the Mid-Atlantic Ridge, on the eastern edge of the southern ridge of Atlantis Massif. Major element and REE concentrations in the one metadolerite sample analyzed from Site M0075 are within the expected ranges of mid-

ocean-ridge basalt: SiO₂ = 47.1 wt%, TiO₂ = 1.1 wt%, Na₂O = 1.9 wt%, Al₂O₃ = 18.2 wt%, MgO = 11.2 wt%, and CaO = 7.9 wt% (Tables T4, T5). The Fe-rich composition (Mg# = 44) is typical of metadolerite across all sites. This metadolerite exhibits a smooth, relatively flat, chondrite-normalized REE pattern with no Eu (Figure F20). As expected, rare earth abundances are elevated relative to other gabbroic and ultramafic lithologies from the eastern sites (Figures F20, F21).

Figure F23. Whole-rock major elements (normalized, volatile-free, and in oxides) vs. MgO for gabbroic and chlorite-rich altered mafic rocks from Atlantis Massif. Data for Mid-Atlantic-Ridge volcanic glass and Expedition 304/305 mafic and ultramafic rocks (Godard et al., 2009) are presented for comparison (<http://www.earthchem.org/petdb>, May 2016).

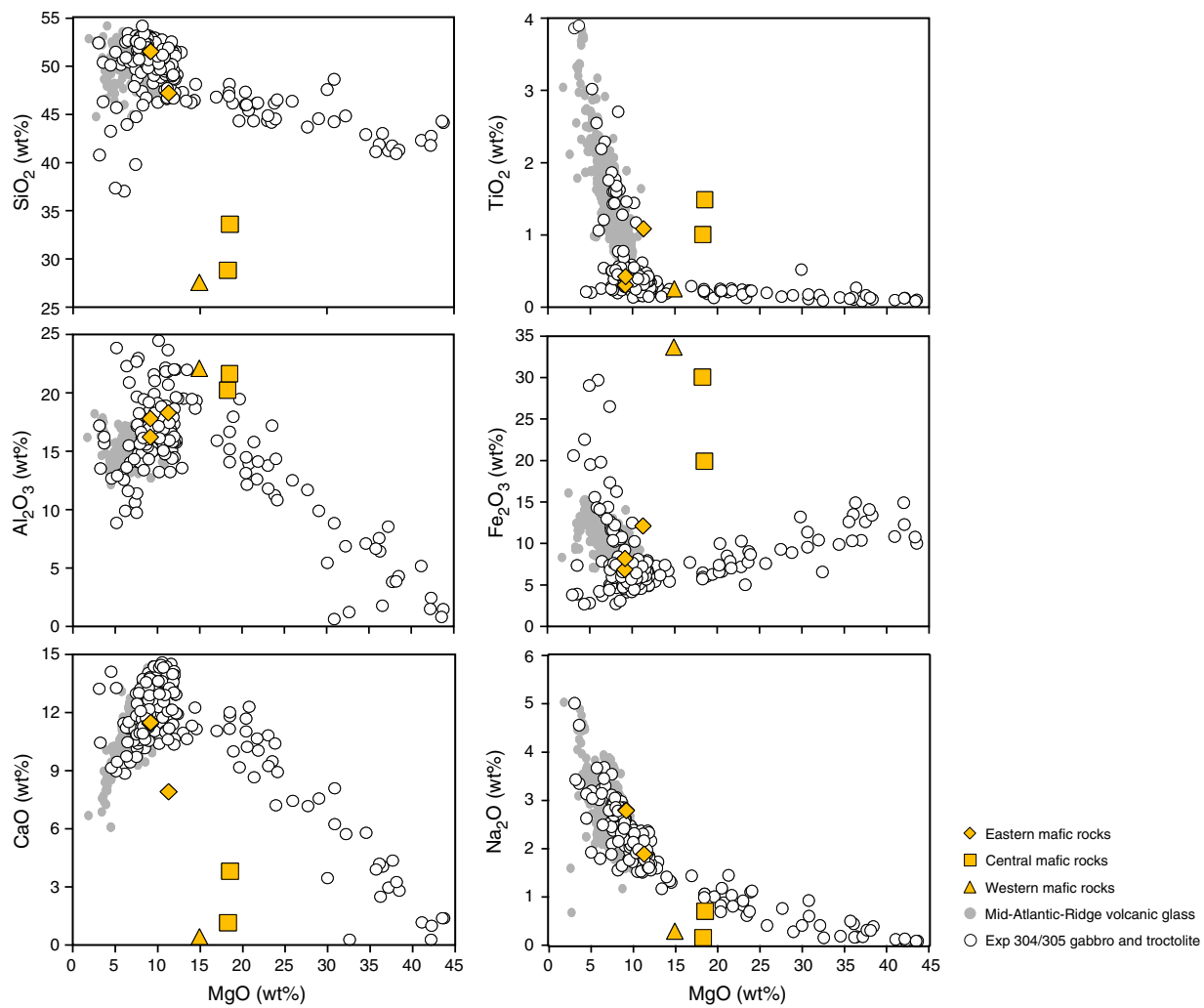
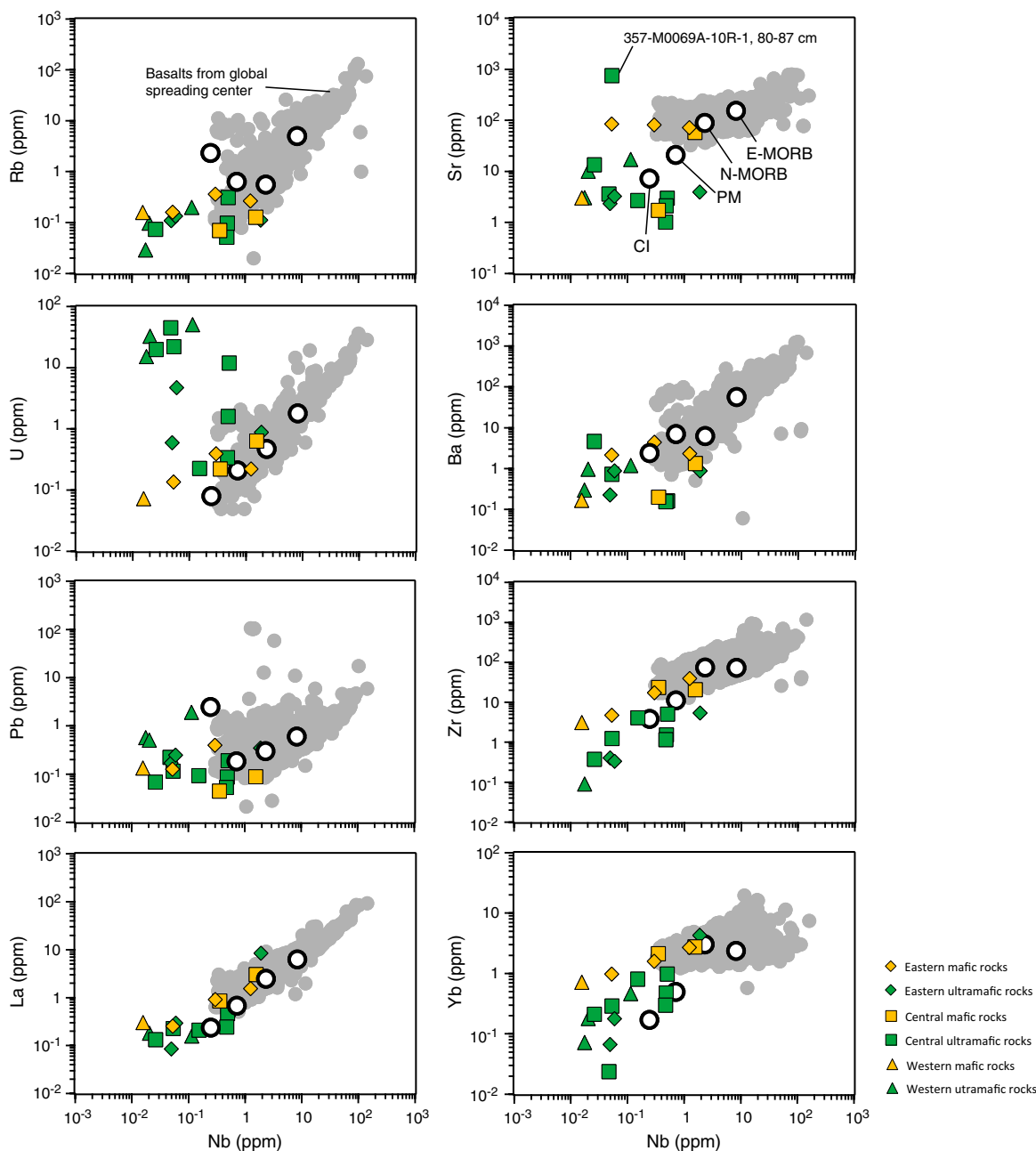


Figure F24. Comparison of Rb, Sr, U, Ba, Pb, Zr, La, and Yb vs. Nb and enriched mid-ocean-ridge basalt (E-MORB), normal MORB (N-MORB), PM, and CI for Atlantis Massif mafic and ultramafic rocks with basalts from global spreading centers, Expedition 357. Data for basalts from global spreading centers (gray dots) from PetDB (<http://www.earthchem.org/petdb>, May 2016). E-MORB, N-MORB, PM, and CI data from Sun and McDonough (1989).



Fluid chemistry

Inorganic and organic fluid chemistry

Offshore fluid chemistry analyses

A total of 40 samples were analyzed at sea for salinity and ammonia from the sensor package (SP) Niskin bottles ($N = 14$), CTD rosette Niskin bottles ($N = 17$), and pore water samples ($N = 9$). Fluid analyses for the entire expedition are reported in one table for each set of data (Table T6) because all measurements were done during single sessions and results were calculated on the basis of the same standard calibration curves. Salinity ranged from 33.2 to 36.4

Table T6. Shipboard salinity and ammonium concentrations measured in fluid samples, Expedition 357. [Download table in .csv format.](#)

in all samples. Significant differences in salinity were not observed between the sensor package Niskin bottles (35.1 ± 0.7), CTD rosette Niskin bottles (35.1 ± 0.7), or pore water (34.5 ± 0.7), nor were significant differences found between the eastern (35.1 ± 0.5), central (35.0 ± 0.8), western (35.1 ± 0.4), and northern (35.0 ± 0.9) sites. In all cases, ammonia concentrations were below detection limits (0.10 ppm).

Cations: major and trace elements

During the expedition, 38 filtered (0.2 μm) and acidified (10 μL of concentrated HNO_3/mL) samples from the sensor package Niskin bottles ($N = 14$), CTD rosette Niskin bottles ($N = 18$), and pore water ($N = 6$) samples were analyzed for cations and trace metals (using a Varian Vista Pro CCD inductively coupled plasma–optical emission spectrometer [ICP-OES] and Agilent Technologies 700 Series ICP-OES, respectively) at the University of Bremen (Germany) (see [Fluid inorganic chemistry analyses](#) in the Expedition 357 methods chapter [Früh-Green et al., 2017b]).

Fluid analyses for major elements and trace elements for the entire expedition are reported in one table for each set of data (Tables [T7](#), [T8](#)) because all measurements were done during single sessions and results were calculated on the basis of the same standard calibration curves. Analyses include 9 samples from the eastern sites (5 CTD and 4 SP), 18 from the central sites (9 CTD, 4 SP, and 5 pore water), 6 from the western sites (2 CTD and 4 SP), and 5 from the northern sites (2 CTD, 2 SP, and 1 pore water). Three duplicate analyses are also reported for each sample type (i.e., 1 CTD, 1 SP, and 1 pore water) (Tables [T7](#), [T8](#)). Quality assurance/quality control (QA/QC) was also based on analyses of standards treated as samples (concentrated standard for major element analyses and Multi 20 and Multi 1 for trace element analyses), blanks (four dispersed throughout the sample list), and International Association for the Physical Sciences of the Oceans (IAPSO) standard seawater. Blank values were generally below detection levels, except for Zn in some of the samples.

Major element results are reported in milligrams per liter (Table [T7](#)), and trace element results are presented in micrograms per liter (Table [T8](#)). These tables also indicate the wavelength selected for each individual element analysis on the ICP-OES. The wavelength selection was carefully carried out by ensuring that

- Measurement areas were centered on the peaks for the concentrated standard analysis,
- The calibration curve was linear (or quadratic) for all standard analyses (five dilution factors for major element analyses and six for trace element analyses) and with minimal error for each element, and
- There was no interference on the measured peak.

Following this QA/QC treatment of the data, all analyzed samples, regardless of collection method (i.e., CTD, SP, or pore water) have comparable major element and trace element concentrations (when above detection) within error of seawater values. This observation was confirmed by comparison with the IAPSO seawater standard. The only exception was that Ca concentrations are lower in the pore water of central Hole M0069A (see [pH, alkalinity, and stable carbon isotope composition of dissolved inorganic carbon](#)). It should be noted that Mn and Ti concentration levels in the samples were below detection limits for the major element method, and Fe and P concentration levels are too low to be reliable. Al concentration levels were too low for the Varian Vista Pro CCD ICP-OES. Many of the trace/minor elements analyzed were below detection levels despite the 10-fold increased sensitivity of the Agilent

Table T7. Concentrations of major elements in fluid samples as measured by ICP-OES, Expedition 357. [Download table in .csv format.](#)

Table T8. Concentrations of trace elements in fluid samples as measured by ICP-OES, Expedition 357. [Download table in .csv format.](#)

Technologies 700 Series ICP-OES. Additionally, there was no peak for P, a major O interference for Rb, Mn interference for Zn, and Sr concentrations were too high (as indicated by “X” in Table [T7](#)); therefore, Sr concentrations were removed from the major element analyses set.

Anions

Aliquots of the same samples were used for anion analysis. After pretreatment and 40-fold dilution, samples were passed through a Metrohm 882 Compact ion chromatograph (about 32 min/sample) for anion analyses (see [Fluid inorganic chemistry analyses](#) in the Expedition 357 methods chapter [Früh-Green et al., 2017b]). The 38 samples and 3 duplicates all matched anion (F, Cl, Br, NO_3 , and SO_4) concentrations of seawater and the IAPSO seawater standard (Table [T9](#)), with the exception of one of the first pore water samples (357-M0069A-1R-1, 5 cm), which had distinctly higher Br levels.

Sulfide

Total sulfide analyses were carried out on the same 38 samples. Nine standard solutions were prepared (from 0.0 to 1.50 ppm) from a new standard solution to build calibration curves. All analyzed samples were below the detection limit of 0.01 ppm (Table [T10](#)).

pH, alkalinity, and stable carbon isotope composition of dissolved inorganic carbon

Unexpected values were obtained from shipboard measurements of pH and alkalinity (see [Fluid inorganic chemistry analyses](#) in the Expedition 357 methods chapter [Früh-Green et al., 2017b]). During the onshore phase, it was determined through rigorous testing with IAPSO seawater salinity standards and freshly prepared alkalinity standards that improper mixing of the samples during titration was the cause of the spurious alkalinity values, despite a magnetic stirrer being used in all measurements offshore. Therefore, alkalinity was measured again during the onshore phase using fluid residues from the water samples. Because pH must be measured immediately after collection, these data unfortunately could not be reproduced. Additionally, the stable isotopic composition of dissolved inorganic carbon (DIC) was measured in a shore-based laboratory on aliquots collected and preserved at sea.

As a substitute for shipboard laboratory measurements of pH on fluid aliquots, pH measurements from the in situ sensor packages were evaluated for the period immediately prior to the drill landing on the seafloor and commencing operations (see [Water sampling and sensor package data](#) in the Expedition 357 methods chapter [Früh-Green et al., 2017b]). These pH ranges are reported in Table [T11](#) as shipboard pH data for bottom water and are presented as an overall summary for the entire expedition. Bottom water pH values determined in this way varied from 7.8 to 7.9.

Similar to other measurements, onshore alkalinity and DIC stable isotope analyses for the entire expedition are reported in one ta-

Table T9. Concentrations of anions in fluid samples, Expedition 357. [Download table in .csv format.](#)

Table T10. Sulfide concentrations in fluid samples, Expedition 357. [Download table in .csv format.](#)

Table T11. pH, alkalinity, and $\delta^{13}\text{C}_{\text{DIC}}$ values for fluid samples, Expedition 357. Reported pH was determined from the average value of the sensor package pH meter mounted on the rock drills, where available. [Download table in .csv format.](#)

ble for each set of data (Table T11) because all measurements were done during single sessions and results were calculated on the basis of the same standard calibration curves. In most locations, fluid samples fell into a narrow range of alkalinity and $\delta^{13}\text{C}_{\text{DIC}}$ values (Table T11; Figure F25). There was no significant difference between the combined average CTD and sensor package Niskin bottle alkalinities or in $\delta^{13}\text{C}_{\text{DIC}}$ between the eastern sites (alkalinity = 2.37 ± 0.03 mM; $\delta^{13}\text{C}_{\text{DIC}} = 0.70\text{‰} \pm 0.17\text{‰}$), central sites (alkalinity = 2.22 ± 0.32 mM; $\delta^{13}\text{C}_{\text{DIC}} = 0.68\text{‰} \pm 0.19\text{‰}$), western sites (alkalinity = 2.37 ± 0.03 mM; $\delta^{13}\text{C}_{\text{DIC}} = 0.65\text{‰} \pm 0.12\text{‰}$), and northern sites (alkalinity = 2.32 ± 0.68 mM; $\delta^{13}\text{C}_{\text{DIC}} = 0.68\text{‰} \pm 0.08\text{‰}$). The one exception is that lower alkalinities were observed in the sediment pore water collected from central Hole M0069A (Figure F25). In these fluids, lower alkalinities were associated with more negative $\delta^{13}\text{C}_{\text{DIC}}$ values and lower calcium concentrations.

Volatile chemistry

Similar to other measurements, offshore analyses of gases for the entire expedition are reported in one table for each set of data (Table T12) because all measurements were calculated on the basis of the same standard calibration curves. A total of 56 water samples for hydrogen and methane analyses were taken using the shipboard

CTD/rosette system. A total of 70 water samples for hydrogen and methane analyses were taken from the sensor package Niskin bottle samples. At the eastern drill sites, methane concentrations were below the detection limit and hydrogen concentrations varied from trace levels to 137 nM. At the central drill sites, methane varied from undetectable to 4 nM and hydrogen varied from 3 to 323 nM. A CTD cast over the Lost City hydrothermal vents (Hole M0072Z), just south of the central drill sites, had significantly elevated methane and hydrogen (35–48 and 196–267 nM, respectively). At the western sites, methane was generally below detection, with the exception of the sensor package Niskin bottle samples collected during operations in Hole M0071A, for which concentrations were roughly 2 nM. Similarly, hydrogen concentrations were also elevated in samples from this hole (32–61 nM compared to <11 nM in other samples). Operations in all three holes at Site M0070 generated samples with methane concentrations of 1–5 nM and hydrogen concentrations of 5–73 nM. Methane and hydrogen were undetectable in fluids from the most northern Site M0074. In summary, hot spots of hydrogen were observed over Sites M0068–M0072, and hot spots of methane were observed over Sites M0070–M0072 (Figure F26).

Figure F25. $\delta^{13}\text{C}_{\text{DIC}}$ vs. alkalinity in CTD, SP, and pore water samples, Expedition 357. Note the larger scale of $\delta^{13}\text{C}_{\text{DIC}}$ for the central sites only. Inset is Ca vs. alkalinity.

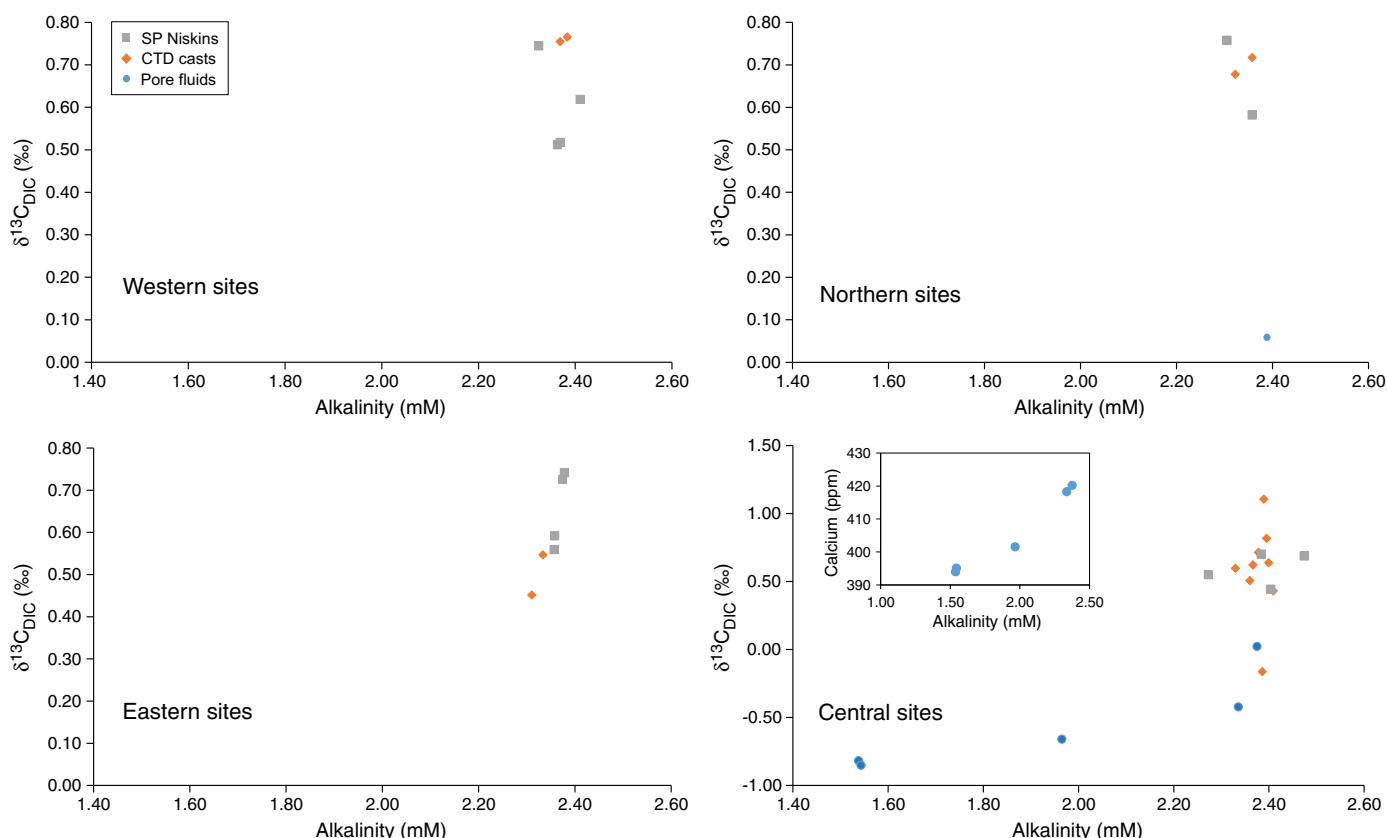
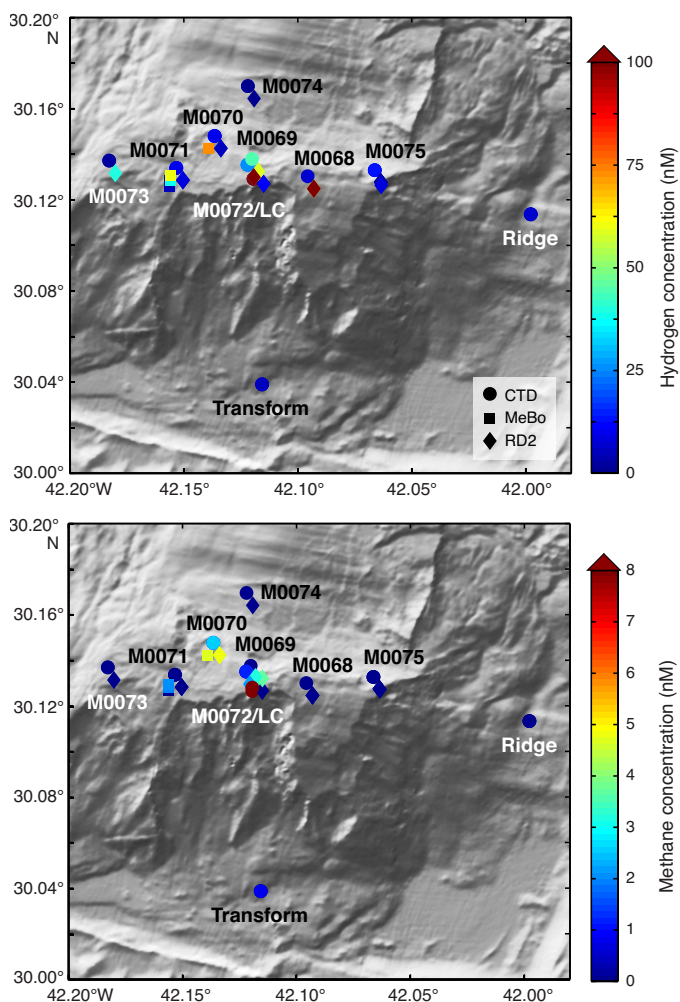


Table T12. Dissolved hydrogen and methane concentrations in CTD rosette water column samples and sensor package Niskin bottle samples compared to penetration depth of the rock drill coring, Expedition 357. [Download table in .csv format.](#)

Figure F26. Highest hydrogen and methane concentrations measured in CTD rosette bottom waters and sensor package Niskin bottles over Atlantis Massif drill sites, Expedition 357. Dark red circles = Lost City (LC) plume samples.



Microbiology

Samples collected

Following the procedure described in detail in [Microbiology](#) in the Expedition 357 methods chapter (Früh-Green et al., 2017b), whole-round core (WRC) samples were transferred to the cold room after they were photographed.

At Site M0068, five WRC samples were collected for microbiological studies: one from Hole M0068A (1R-1) and four from Hole M0068B (1R-1, 3R-1, 7R-1, and 8R-1) (Table T13; see MBIOWRC in [Supplementary material](#)). Centimeter-sized rock pieces were flame sterilized for interior perfluoromethylcyclohexane (PFC) tracer, cell count, and single-cell samples, but because of the limited amount of material, no larger pieces from this site were flame sterilized for bulk nucleic acid extraction. Additional rock pieces from Section 357-M0068B-5R-1 were collected for PFC tracer check, cell count, and gas analyses. In summary, five unflamed frozen samples, three enrichment samples, five exterior PFC samples, four interior PFC samples, five gas analyses samples, four exterior cell count

Table T13. Whole-round cores collected for microbiological analysis, Sites M0068 and M0075. [Download table in .csv format.](#)

samples, four interior cell count samples, and four single-cell analysis samples were collected. Additional exterior cell count samples were taken at the top of Sections 2R-1, 3R-1, 5R-1, and 8R-1 and adjacent to microbiology whole-round samples in Section 3R-1.

At Site M0075, three WRC samples were collected for microbiological studies: one from Hole M0075A (1R-CC) and two from Hole M0075B (2R-1 and 3R-1). Flamed WRC samples for nucleic acid extraction were taken from the two Hole M0075B sections, but no flamed sample was taken from Hole M0075A because of the limited sample volume. Additionally, we took at least one sample for exterior and interior PFC tracer check, exterior and interior cell count, CH₄/H₂ gas analysis, shipboard enrichment/incubation, and single-cell genome sequencing; we did not sample for interior cell count and single-cell genome sequencing for Hole M0075A because of the limited sample volume.

Samples sent to Kochi Core Center (Japan) were immediately frozen at -80°C and then shipped under temperature-controlled conditions with constant temperature logging. There, WRC exteriors were cut away with a band saw system equipped in a clean booth and used for PFC tracer check (exterior), concentration and isotopic composition of TIC/TOC, vein analysis, in situ organic carbon and Fe mineral analysis, and trapped-gas analysis. The interior portions of the frozen samples were subjected to shore-based nucleic acid analyses and interior PFC, amino acid, and lipid analyses.

Liner fluid from the core barrels was collected from Sections 357-M0068A-1R-1, 357-M0068B-1R-1, 3R-1, 6R-1, 7R-1, and 8R-1 and 357-M0075A-1R-1, 2R-1, and 3R-1 and split for PFC, cell count, and organic acid analyses (Table T14).

Contamination assessment with PFC tracer

Samples of core barrel liner fluids, sensor package Niskin bottles, and exterior and interior pieces of WRC were collected for assessing potential of contamination by quantifying the concentration of PFC tracer added during drilling operations (see [Microbiology](#) in the Expedition 357 methods chapter [Früh-Green et al., 2017b]). Because samples collected throughout the expedition were measured in batches against the same standard calibration curves, data for the entire expedition are reported in Table T15. Laboratory atmosphere blanks are also reported to define lower detection limits; these values varied throughout the expedition due to buildup of volatilized tracer in the shipboard laboratory. PFC concentrations for samples are reported in picograms PFC per cubic centimeter of sample, and laboratory blanks are reported as picograms PFC per milliliter air.

PFC delivery during drilling operations in Hole M0068B was weak based on very low concentrations (<100 pg PFC/mL sample) of tracer in the sensor package and liner fluid samples (Table T15). No samples were collected from the WRC from this hole. PFC delivery during drilling operations in Hole M0068B was very successful, with high to saturating concentrations of PFC in the sensor package Niskin samples, liner fluid samples, and WRC exterior. Interior samples from the WRC also have high PFC concentrations, indicating that flaming the exterior of the WRC was not sufficient to remove the tracer. This result is not unexpected, as the WRCs collected for microbiology from this hole were not very coherent

Table T14. Core liner fluid samples for microbiological analyses, Sites M0068 and M0075. [Download table in .csv format.](#)

Table T15. PFC tracer concentrations, assessment of rock drill tracer delivery conditions, and laboratory lower detection limits, Expedition 357. [Download table in .csv format.](#)

but rather predominantly rubbly and composed of talc schist (see MBIOWRC in [Supplementary material](#)). PFC tracer delivery during drilling operations in Holes M0075A and M0075B was also mostly successful, although concentrations in the sensor package Niskin bottles and liner fluids are lower than those from Hole M0068B. WRC exteriors, which are also mostly rubbly or unconsolidated material, have relatively high concentrations of PFC. WRC interiors also contain PFC but generally at 1–2 orders of magnitude lower concentration than the exteriors.

Cell abundance determination

Cell abundance was determined by direct counting with an epifluorescence microscope (see [Microbiology](#) in the Expedition 357 methods chapter [Früh-Green et al., 2017b]). For shipboard analysis of select rock samples, flame-sterilized interior cell count samples were crushed into millimeter-sized grains, and then 3 cm³ was taken for fixation. Minimum quantification limits of the cell counting methods were determined by analysis of procedural negative controls and determined to be 48 cells/cm³.

For the eastern sites, cell abundance was found to be very low in the select samples analyzed (Table T16). In the uppermost sample from Hole M0068B (1.4 mbsf), cell density was $\approx 7.1 \times 10^3$ cells/cm³. Cell abundance decreased rapidly with depth and was below minimum quantification limit at 7 mbsf. No samples from Site M0075 were analyzed on the ship, but they will be investigated in shore-based laboratories.

Enrichment and incubation experiments

The growth and activity of microbial communities was studied in rock samples obtained during the expedition using a variety of culture-based approaches. Flame-sterilized pieces of rock material were ground to fine particles under anoxic conditions and distributed into the various incubation vessels (Table T13; see [Microbiology](#) in the Expedition 357 methods chapter [Früh-Green et al., 2017b]).

Samples were used in the following ways:

- To study the activities of microorganisms and extracellular enzymes (Section 357-M0068B-1R-1),
- To study the growth of microorganisms under sulfate reducing conditions (Section 357-M0068B-3R-1),
- To study microbe-rock interactions (Sections 357-M0068B-7R-1, 357-M0075A-2R-1),
- To study the assimilation of stable isotope-labeled carbon and nitrogen compounds (Section 357-M0075A-1R-CC), and
- To investigate the growth of anaerobic microbes under elevated hydrostatic pressure conditions (Section 357-M0075B-3R-1).

Water samples for microbiological analysis

Water from sensor package Niskin bottles and CTD rosette Niskin bottles was sampled for measurements of PFC, cell counts, and DNA from Sites M0068 and M0075 (Tables T17, T18) and for many

Table T16. Microbial cell abundance counted on flame-sterilized interior piece of rock samples, Site M0068. [Download table in .csv format.](#)

Table T17. Water samples collected from sensor package Niskin bottles for microbiological analysis, Sites M0068 and M0075. [Download table in .csv format.](#)

Table T18. Water samples collected from CTD rosette Niskin bottles for microbiological analysis, Sites M0068 and M0075. [Download table in .csv format.](#)

chemical measurements (see [Water sampling and sensor package data](#) in the Expedition 357 methods chapter [Früh-Green et al., 2017b]).

Sensor package data

The variability in temperature, pH, CH₄, oxidation-reduction potential (ORP), and, in some instances, dissolved O₂ detected by the rock drill sensors is described below for the eastern sites. Mapping drill data onto the sensor plots for all sites was done graphically, and for records of approximately 1000 min, potential errors are on the order of ± 5 min. In summary, pH increased downhole at each site and CH₄ background levels were variable, ranging from 0.1 to 58 nM with the highest values found at eastern Site M0075. Significant downhole CH₄ peaks were common at most sites. ORP minima were very common, with at least two causal mechanisms: (1) associated with specific horizons during continuous drilling of a specific core and (2) caused by the shutting off of flushing water, which reduced the dilution of formation fluid as core barrels were changed. Temperature was variable (typically by a few tenths of a degree but up to 1°C at some sites) but difficult to interpret due to the potential for heating by the drill. Background values were on the order of 7.8 for pH and about 340 mV for ORP. Background temperatures were variable with depth and ranged from 5° to 10°C.

It must be noted that the METS CH₄ sensor has some sensitivity to molecular H₂, and because we expected significant H₂ concentrations in the Atlantis Massif environment, we asked Franatech to evaluate this potentially interfering response level. The results of these tests indicate that the sensor has 0.02 times the sensitivity to H₂ as it does to CH₄. Thus, when a signal from the METS sensor is described, the signal likely represents a combination of H₂ and CH₄. Because the METS sensor is a membrane device, there is also a delay in the response time, and a step change in concentration takes on the order of 1–2 min for 90% response.

Hole M0068A

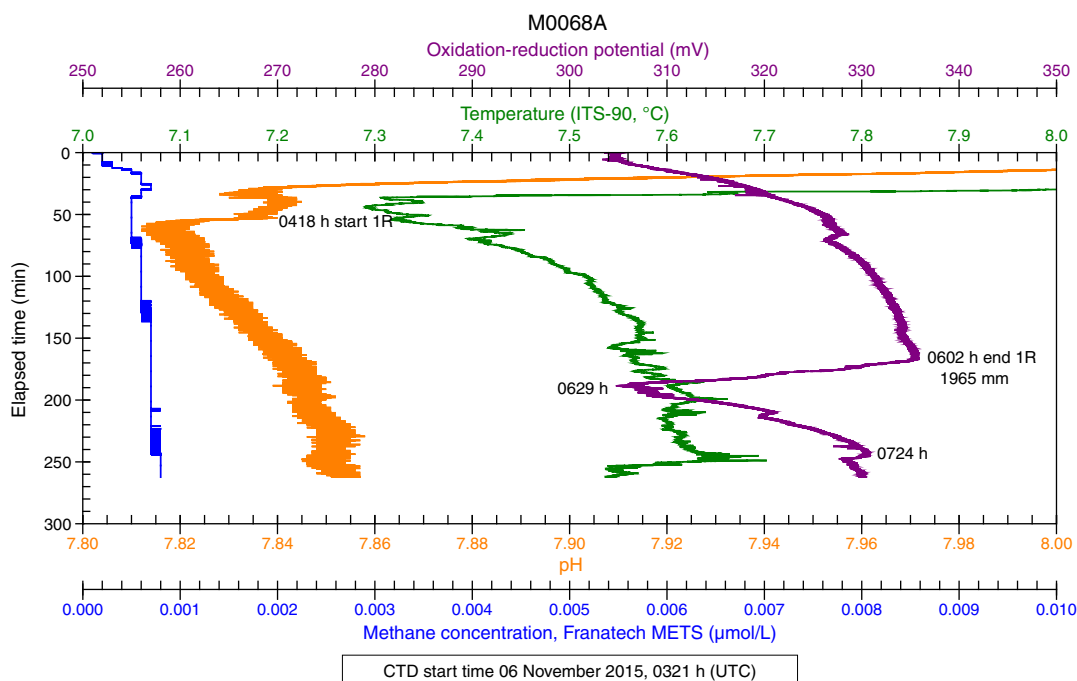
Because of a malfunction of the data logger on the RD2 while drilling Hole M0068A, we were not able to correlate sensor signals with specific depths. This is a shallow hole with only one core, and drilling ended at 0602 h. Other than a general increase in pH downhole and a negative ORP excursion that began at the cessation of drilling, no major sensor anomalies were associated with this hole (Figure F27; Table T19). This ORP excursion is likely the result of cessation of flushing and dilution of the formation water. CH₄ background values range from about 0.4 to 0.7 nM, which is about the local seawater background value. Typical of all the sites, pH values increased downhole (Figure F28).

Hole M0068B

Because of a malfunction of the data logger on the RD2 while drilling Hole M0068B, we were not able to correlate sensor signals with specific depths. We can, however, place such signals within specific cores, and the depths shown on the figures for this hole represent depths and start and end times for each core. As a result of a power recycle, sensor data for this hole were divided into two separate files and are represented by separate plots.

The first sensor data section (Figure F28A), which covers the first four cores, depicts several negative excursions in ORP while drilling within specific core sections. The negative ORP peak centered within Core 1R implies that a zone of more reducing fluids was encountered while drilling. Although data on the flushing rate

Figure F27. Sensor data, Hole M0068A. Elapsed time = time since the start of the sensor package data file. Penetration depth is from drill logs.

Table T19. Sensor signal time log, Hole M0068A. [Download table in .csv format.](#)

during drilling is not available for operations at this site to examine whether changes in flushing rate could correlate to this ORP excursion, drilling video confirms that there was no change in drill rods at the time of the excursion (flushing stops during rod uncoupling). Two negative ORP peaks at 0456 and 0534 h (UTC – 2 h) occurred within Core 3R. The drill logs note that a drill rod was added while drilling Core 3R, and the video shows the drill rods uncoupled and flushing stopped at 0600 h. The rods were recoupled (flushing restarted) at 0610 h, and this operation resulted in only a small blip in the ORP signal. Thus, the negative excursion of the ORP signal appeared to be inherent to the formation while drilling Core 3R. While drilling Core 4R, no additional drill rods were needed; thus the minimum in the ORP signal at 0947 h was inherent to the formation and not related to drilling operations. Between the end of Core 4R at 1152 h and the start of Core 5R at 1440 h, the drillers experienced difficulties, and several instances of uncoupling/recoupling drill rods would have stopped and restarted the flushing water as well. These events produced no major sensor signal deviations. There were no CH₄ anomalies while drilling the uppermost four cores in Hole M0068B, and background values were around 1 nM. However, as we saw at virtually all sites, there was a slight pH increase downhole.

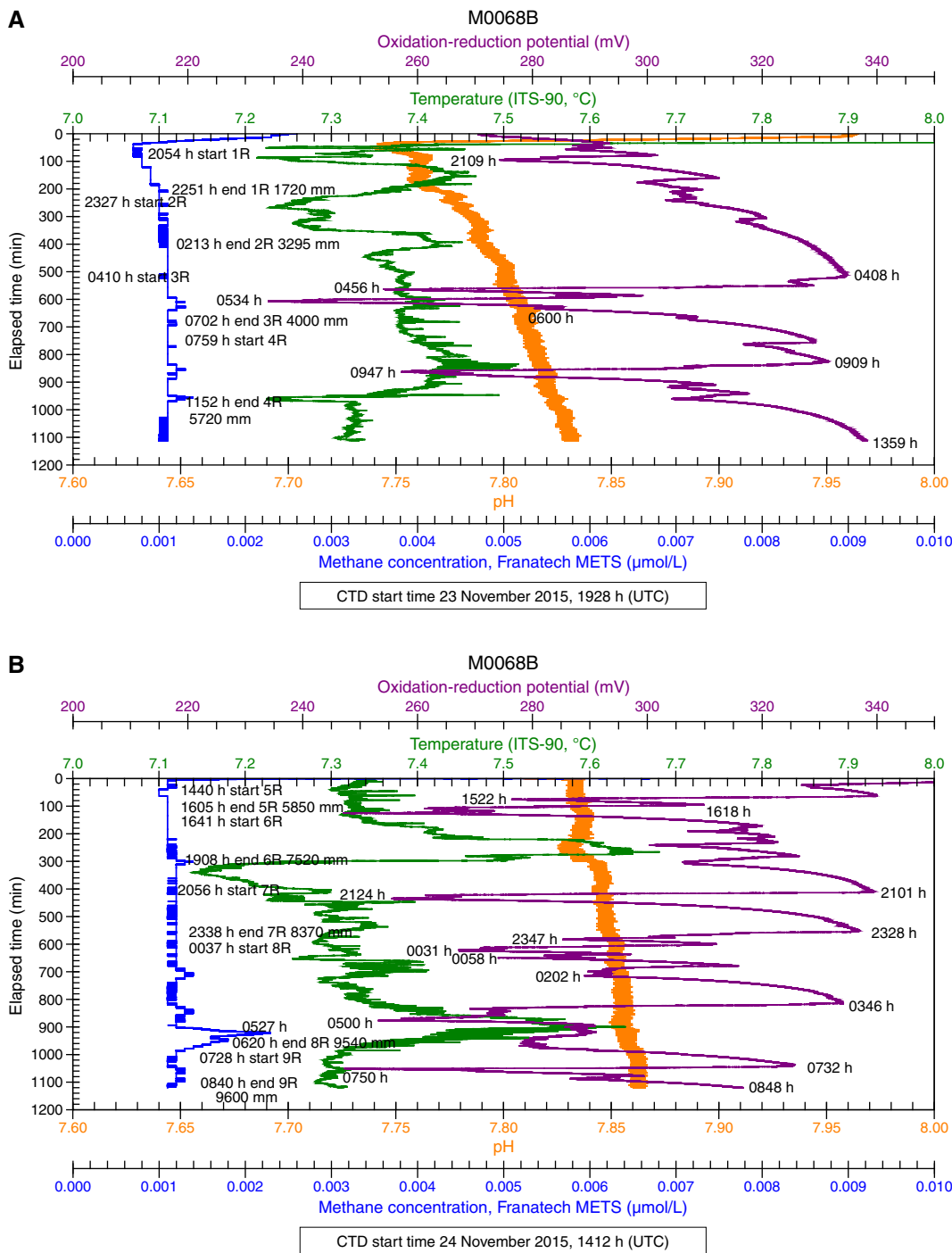
The sensor data associated with the lowermost five cores from this hole are shown in Figure F28B. The negative ORP excursion, which reached a minimum at 1522 h, occurred within Core 5R with no stoppage of hole flushing during this period. However, the second, more pronounced excursion, reached a minimum at 1618 h during the period of recovery of Core 5R when no flushing was taking place, indicating that we were sampling reduced fluids from the hole without the added dilution brought about by flushing the hole. While drilling Core 6R, no additional drill rods were added, and the only significant change in sensor signals was a 0.3°C increase in

temperature, which is difficult to interpret with frictional heating from the drill a possibility. Drilling of Core 7R started at 2056 h, and at 2107 h a negative ORP excursion started and reached a minimum at 2124 h. This minimum was reached several minutes prior to the uncoupling of the drill rods (flushing stopped) at 2146 h. The ORP signal continued to increase throughout the remainder of Core 7R and reached a background value near 340 mV at 2328 h, coincident with the completion of Core 7R. There was a series of ORP minima before and while drilling Core 8R. One such negative excursion started at 2328 h, coincident with the end of Core 7R when the flushing water would have been turned off. Two ORP minima were reached at 2350 and 0031 h, prior to the start of Core 8R at 0037 h. Two more ORP minima (at 0058 and 0202 h) were seen prior to stopping drilling to add a drill rod at 0230 h. Drilling commenced again at 0250 h, and another large negative ORP excursion started at 0346 h, reaching a minimum at 0500 h. Drilling of Core 9R started at 0728 h, almost simultaneously with the beginning of a negative ORP excursion that reached a minimum at 0750 h. This ORP excursion was likely formation-derived because no extra drill rod was added while drilling this core. Although less pronounced than in the upper four cores, pH continued to increase downhole. Background CH₄ values were about 1.2 nM, but a small anomaly (2.4 nM) was seen at 0527 h within Core 8R. A summary of drilling information associated with the sensor logs from this hole is given in Table T20.

Hole M0075A

Hole M0075A is a short, one-core hole with a water depth too deep to allow the use of the pH/ORP sensor. A dissolved oxygen decrease and temperature increase started simultaneously with the drilling of Core 1R and reached a minimum/maximum 8 min later at 154 mm. The event remained more or less constant until 1310 h (1429 mm), 5 min prior to the completion of Core 1R (Figure F29; Table T21). The drill-flushing rate was constant throughout the drilling of this core, so it appears a zone with higher temperature and lower oxygen was encountered during drilling, although the

Figure F28. Sensor data, Hole M0068B. Elapsed time = time since the start of the sensor package data file. Penetration depth is from drill logs. A. Cores 1R–4R. B. Cores 5R–9R.



amount of heating due to the drilling process is unknown. CH₄ was relatively high, ranging from 56 to 57.5 nM with a small jump that coincided with the end of Core 1R. Drill rotation and flushing stopped at 1319 h, and the drill lifted off bottom at 1409 h.

Hole M0075B

As in Hole M0075A, the pH/ORP sensor could not be used in Hole M0075B because of water depth. A set of anomalies (tempera-

ture minimum, oxygen maximum, and a small CH₄ maximum) occurred at 2259 h while drilling Core 2R (Figure F30). The only drilling anomaly around this time was a 16 s stop of drill rotation; the flush rate was fairly constant at about 26 L/min throughout the period (Table T22). There was also a small temperature increase associated with the start of Core 3R. CH₄ levels were relatively high throughout drilling, ranging from 54 to 58 nM.

Table T20. Sensor signal time log, Hole M0068B. [Download table in .csv format.](#)

Figure F29. Sensor data, Hole M0075A. Elapsed time = time since the start of the sensor package data file. Penetration depth is from drill logs.

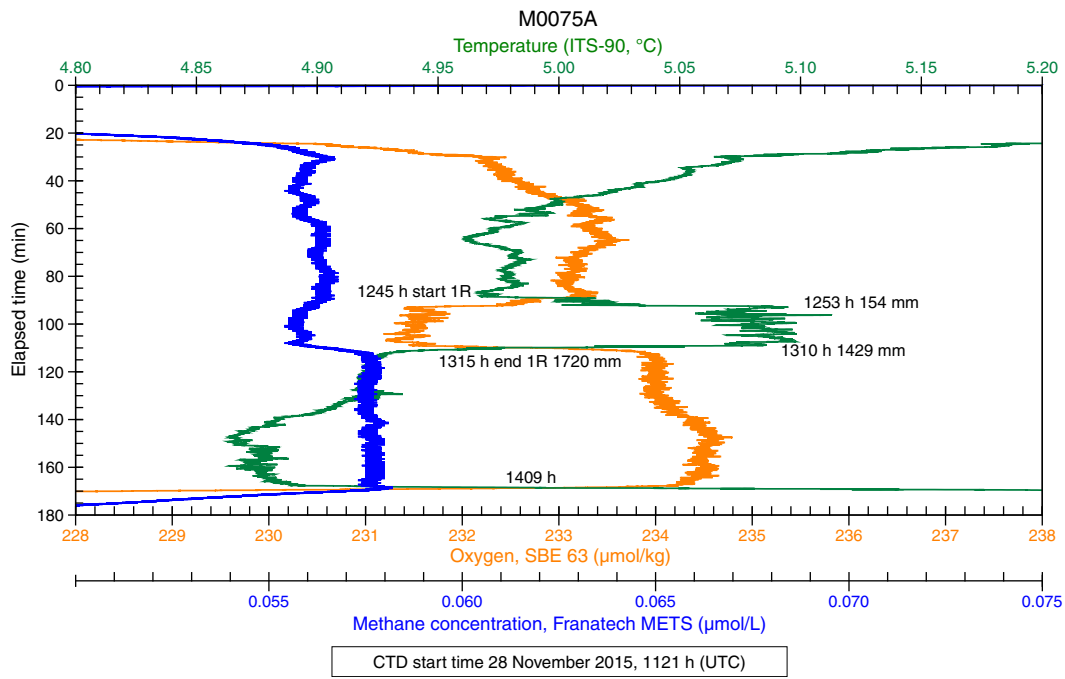


Table T21. Sensor signal time log, Hole M0075A. [Download table in .csv format.](#)

Figure F30. Sensor data, Hole M0075B. Elapsed time = time since the start of the sensor package data file. Penetration depth is from drill logs.

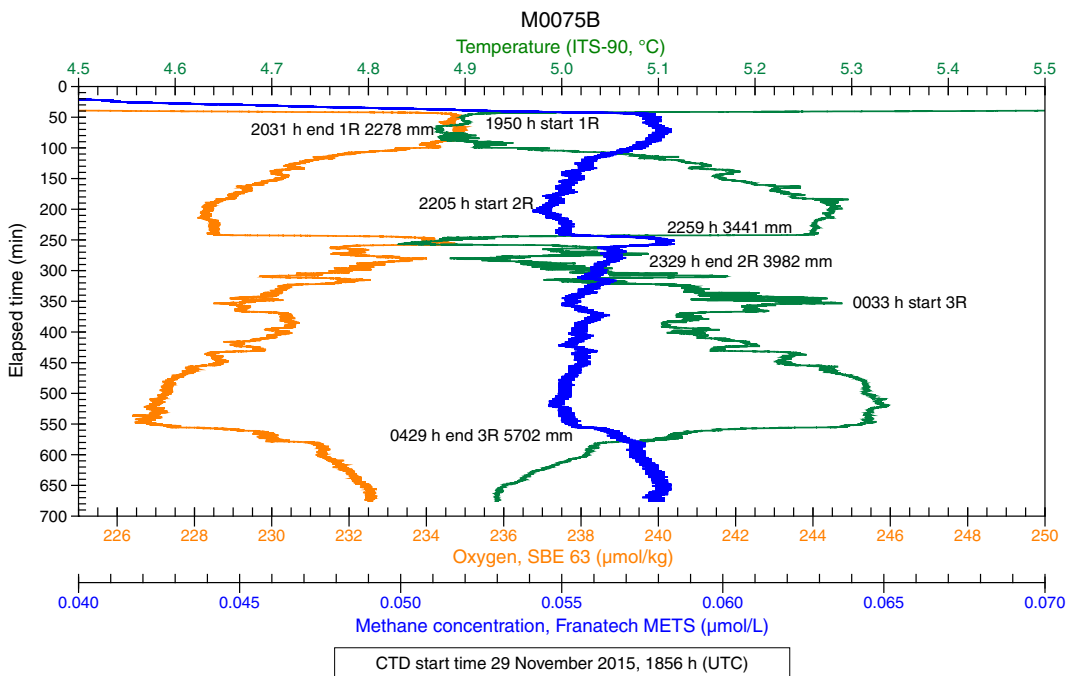


Table T22. Sensor signal time log, Hole M0075B. [Download table in .csv format.](#)

Borehole plugs

After RD2 drilling operations at the eastern sites, two attempts were made to install borehole plugs. For further details on borehole plugs, see **Borehole plugs** in the Expedition 357 methods chapter (Früh-Green et al., 2017b).

After tripping out the drill string in Hole M0068B, a short borehole plug system was inserted into the open hole (Figure F31). The borehole plug consisted of a 2.17 m length of titanium tube with a ball-valve assembly at the upper end connected to a packer element below. A stop ring on the titanium pipe was set 1.02 m from the top of the assembly. Penetration reached 9.6 mbsf; the borehole plug assembly was targeted to reach 2.25 mbsf if inserted as planned, and the packer element was set below 1.15 m. During liftoff of the RD2 drill rig, the top part of the assembly became stuck in the breakout

table of the drill rig and was lifted out of place by an unknown amount. It is unclear if the borehole plug fell back into place or was left partially or completely out of the hole.

After tripping out the drill string in Hole M0075B, a short borehole plug system was inserted into the open hole (Figure F32). The borehole plug consisted of a 2.17 m length of titanium tube with a ball-valve assembly at the upper end connected to a packer element below. A stop ring on the titanium pipe was set 0.36 m from the top of the assembly. Penetration reached 5.7 mbsf. The system did not penetrate to the target depth because of resistance, but the packer element is below the seafloor, beginning at roughly 1.25 mbsf, with a final penetration of 2.35 m. The liftoff of the drill rig from the system stick up went well, and the top of the plug system likely sits about 0.92 m above the seafloor.

Figure F31. Borehole plug emplacement, Hole M0068B. The plug may not be set in the seafloor as drawn because the assembly was pulled out of the hole during liftoff of the RD2.

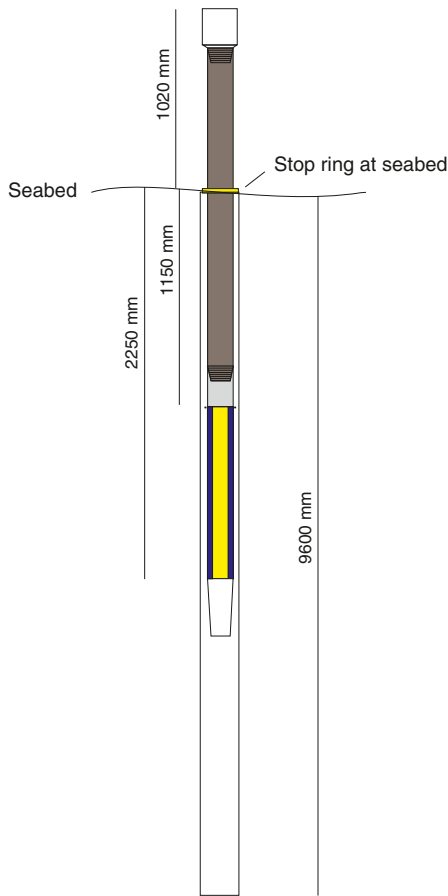
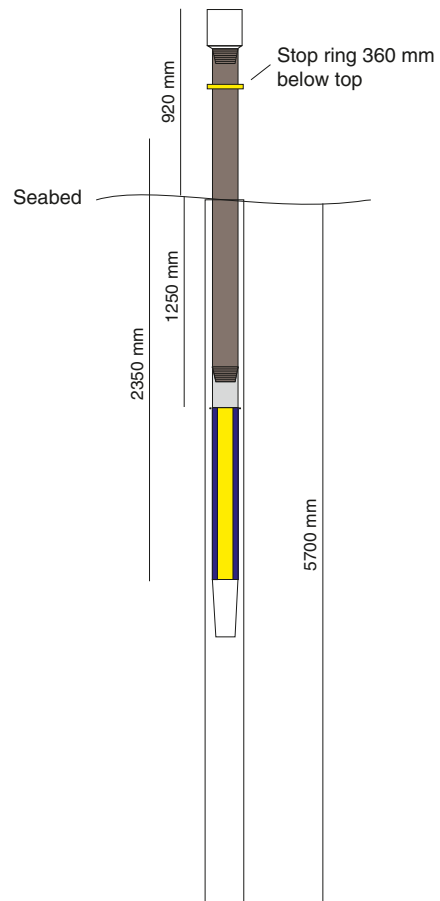


Figure F32. Borehole plug emplacement, Hole M0075B.



Physical properties

Site M0075

Two holes were cored at Site M0075 with a combined recovery of 3.38 m: $\approx 38\%$ in the shallower (1.72 mbsf) Hole M0075A and $\approx 48\%$ in the deeper (5.70 mbsf) Hole M0075B.

Density and porosity

Gamma density (GD) is 2.36 g/cm^3 on average, varying between 1.65 and 2.63 g/cm^3 (Table T23; Figures F33, F34). The lowest values are concentrated at the tops and bottoms of core sections. Scatter in the gamma density profile is principally related to the degree of fragmentation of the core and, more generally, core quality. The low densities at the top and bottom of Section 357-M0075B-2R-1 (2.28–3.21 mbsf), for example, correspond to rubbly intervals, compared to a fragmented but more compact segment with higher densities in the center.

One discrete sample was taken from Site M0075 for moisture and density (MAD) analysis (see **Physical properties** in the Expedi-

Table T23. Physical properties on discrete samples, Sites M0075 and M0068. [Download table in .csv format.](#)

tion 357 methods chapter [Früh-Green et al., 2017b]). The talc-chlorite schist sample (357-M0075A-1R-CC, 10–12 cm; 0.62 mbsf) has a grain density of 2.82 g/cm^3 , and its porosity is 4.5% (Figure F35).

P-wave velocity

One oriented sample from Hole M0075A was measured for tri-axial *P*-wave velocity. The talc-chlorite schist sample has a mean *x*-direction velocity of 4.48 km/s (Table T24). A higher value of 4.62 km/s was measured on the sample after trimming the lower end face of the cylinder to improve contact with the transducer pads. The second horizontal direction is the *y*-direction. These measurements yielded higher *P*-wave velocities (5.53 km/s wet; 4.75 km/s dry) with a mean of 5.14 km/s . *P*-wave velocities measured along the *z*-direction (vertical) are 4.71 km/s wet and 3.85 km/s dry with a mean of 4.28 km/s . The measurements on this sample show lower velocities in the dry state along the *y*- and *z*-directions, which may reflect less effective acoustic coupling with the transducer pads in the dry state. The higher *P*-wave velocity measured dry along the *x*-direction is probably due to improved acoustic coupling from trimming the lower cylinder face. In principle, the differences measured in the *x*-, *y*-, and *z*-directions may be a reflection of the true acoustic

Figure F33. Physical properties from core scanning and discrete samples, Hole M0075A. MAD: red circle = bulk density, green circle = dry density, blue circle = grain density. *P*-wave velocity: open square = *z*-direction, open circle = *x*-direction, blue dot = *y*-direction. Color reflectance: black = L^* , red = a^* , blue = b^* .

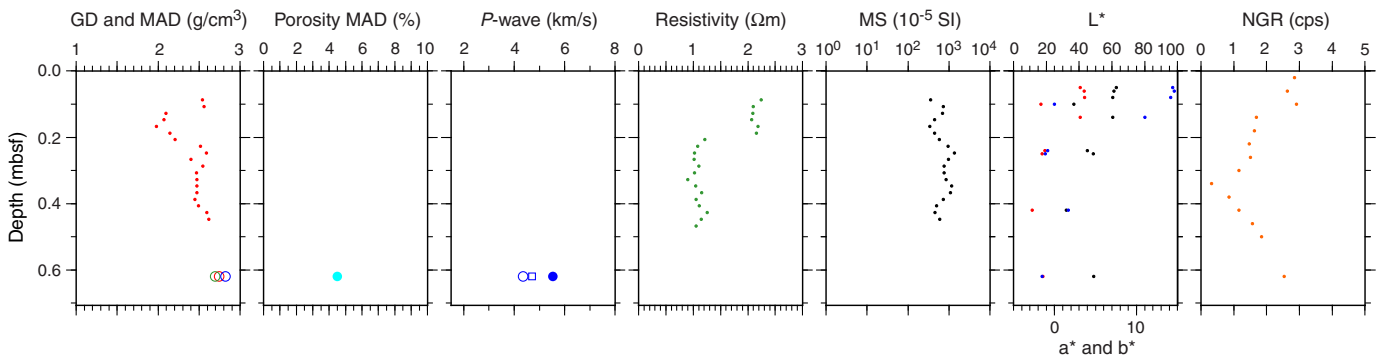


Figure F34. Physical properties from core scanning, Hole M0075B. Color reflectance: black = L^* , red = a^* , blue = b^* . No discrete samples were analyzed.

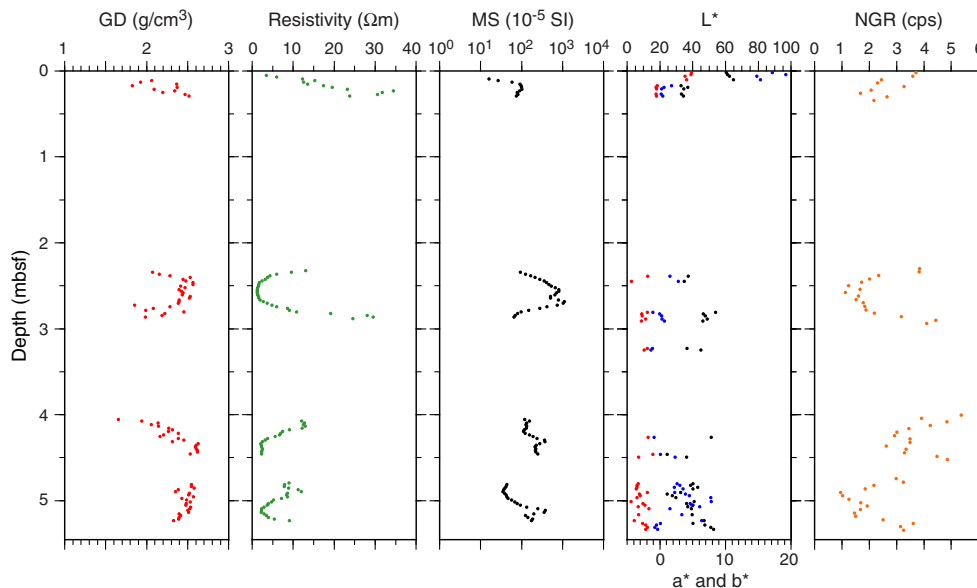


Figure F35. Grain density and porosity data from MAD analyses, Sites M0075 and M0068. Lithologies are defined by core description (see [Lithology, alteration, and structure](#)).

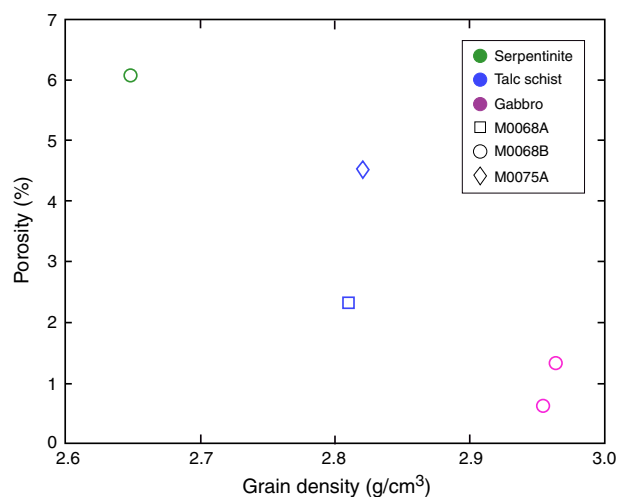


Table T24. Grain density, porosity, and *P*-wave velocity of discrete samples, Sites M0068 and M0075. [Download table in .csv format](#).

anisotropy of the sample. However, this cannot be quantified on the basis of measuring in three directions because the orientation of the three principal axes of acoustic anisotropy is not known.

Electrical resistivity

Electrical resistivity data from Site M0075 cores has a mean of 7.1 Ω m, a minimum of 0.9 Ω m, and a maximum of 34.5 Ω m (Figures F33, F34; Table T23). Local maxima are located at 0.2, 2.3, 2.9, 4.1, 4.9, and 5.2 mbsf. In general, resistivity negatively correlates with magnetic susceptibility.

Magnetic susceptibility

Magnetic susceptibility (MS) is low, with a mean of 332×10^{-5} SI, a minimum of 16×10^{-5} SI, and maximum of 1360×10^{-5} SI (Figures F33, F34; Table T23). In Hole M0075A, which only reaches 0.5 mbsf, magnetic susceptibility is higher than it is at the equivalent depth in Hole M0075B (maximum = 1360×10^{-5} SI compared to 34×10^{-5} SI in Hole M0075B). However, this discrepancy matches the change in lithologies between the two holes (sedimentary breccia with basaltic and talc-rich clasts in Hole M0075A and basaltic clasts in Hole M0075B) (see [Lithology, alteration, and structure](#)).

Natural gamma radiation

Natural radioactivity was measured on all Site M0075 cores (Figures F33, F34; Table T23). Natural gamma radiation (NGR) is very low, which is characteristic of the lithologies sampled. Hole M0075A has an NGR minimum at 0.34 mbsf. Of the three Hole M0075B cores, Core 2R exhibits the lowest and least variable NGR, and Core 3R is far more variable along its length. Absolute values are not reported here because the units are uncalibrated.

Color reflectance

In Hole M0075A, the mean lightness (L^*) is 50.67%, varying between 32.19% and 62.73% (Table T23; Figure F33). Mean values of a^* and b^* are 0.55 (ranging from -2.73 to 3.65) and 5.81 (ranging from -1.54 to 14.61), respectively. In this hole, where only one 0.65

m core was recovered, color reflectance could only be measured at a few points because of the highly fractured and heterogeneous nature of the material (see [Physical properties](#) in the Expedition 357 methods chapter [Früh-Green et al., 2017b]). The scattered L^* , a^* , and b^* values reflect this heterogeneity.

In Hole M0075B, L^* varies between 24.37% and 64.88% with a mean value of 41.93% (Table T23; Figure F34). a^* ranges from -4.41 to 4.82 (mean = -1.75), and b^* ranges from -1.39 to 19.22 (mean = 3.40). The large variations observed are possibly due to the fine-scale heterogeneity and rubby structure in this hole.

Site M0068

Two holes were drilled and cored at Site M0068. Recovery was significantly better in Hole M0068B (66%), the deeper hole (≈ 9.6 m), than in the shallower (≈ 1.9 m) Hole M0068A ($\approx 24\%$).

Density and porosity

Site M0068 cores have a mean gamma density of 2.32 g/cm^3 (Table T23; Figures F36, F37). Values range between 1.47 and 2.74 g/cm^3 . The highest densities are concentrated above 1.2 mbsf and between 3.5 and 5.6 mbsf. This profile roughly follows the trend of magnetic susceptibility (see below). The lowest densities are lower than expected for the corresponding lithologies and lower than the densities determined on discrete samples. These low densities are probably related to core quality.

Four discrete samples for MAD and *P*-wave velocity measurements were taken at Site M0068 (Figure F35): two gabbroic rocks, one serpentinite, and one talc-amphibole schist. The gabbros have similar grain densities of 2.96 and 2.95 g/cm^3 but different porosities of 1.3% and 0.6% at 1.33 and 2.00 mbsf, respectively. This discrepancy may be caused by more intense alteration at 1.33 mbsf, as evidenced by a higher proportion of amphibole compared to clinopyroxene than that found at 2.00 mbsf (see [Lithology, alteration, and structure](#)). Grain density and porosity are 2.65 g/cm^3 and 6.1%, respectively, for the serpentinite sample (4.22 mbsf) and 2.81 g/cm^3 and 2.3%, respectively, for the talc-amphibole schist sample (0.31 mbsf).

P-wave velocity

Four discrete samples were obtained from Site M0068 cores (Table T24). The two samples of gabbroic rock have the highest velocities in all directions. Repeated measurements on Sample 357-M0068B-1R-1, 133–135 cm, resulted in *P*-wave velocities of 5.63 and 6.99 km/s (*x*-direction, mean = 6.31 km/s), 4.29 and 5.66 km/s (*y*-direction, mean = 4.97 km/s), and 6.11 and 5.51 km/s (*z*-direction, mean = 5.81 km/s). These figures highlight the limits to repeatability of the measurements. The higher value recorded in the *x*-direction in the second measurement is due to improved acoustic coupling following trimming of the lower cylinder face. Sample 2R-1, 28–30 cm, yielded *x*-direction measurements of 5.68 km/s (wet, untrimmed lower cylinder face) and 5.88 km/s (dry, trimmed lower cylinder face) with a mean *x*-direction velocity of 5.78 km/s. Measurements along the *y*-direction result in higher *P*-wave velocities (8.56 km/s wet; 8.16 km/s dry) with a mean of 8.36 km/s. *P*-wave velocities measured along the *z*-direction (vertical) are 8.62 km/s wet and 8.23 km/s dry with a mean of 8.42 km/s. As discussed above, the wet and dry measurements on this sample show lower velocities in the dry state along the *y*- and *z*-directions, which may reflect less effective acoustic coupling with the transducer pads in the dry state. The overall mean of all readings for Sample 1R-1, 133–135 cm, is 5.70 km/s; for Sample 2R-1, 28–30 cm, it is 7.52 km/s.

Figure F36. Physical properties from core scanning and discrete samples, Hole M0068A. MAD: red circle = bulk density, green circle = dry density, blue circle = grain density. P -wave velocity: open square = z -direction, open circle = x -direction, blue dot = y -direction. Color reflectance: black = L^* , red = a^* , blue = b^* .

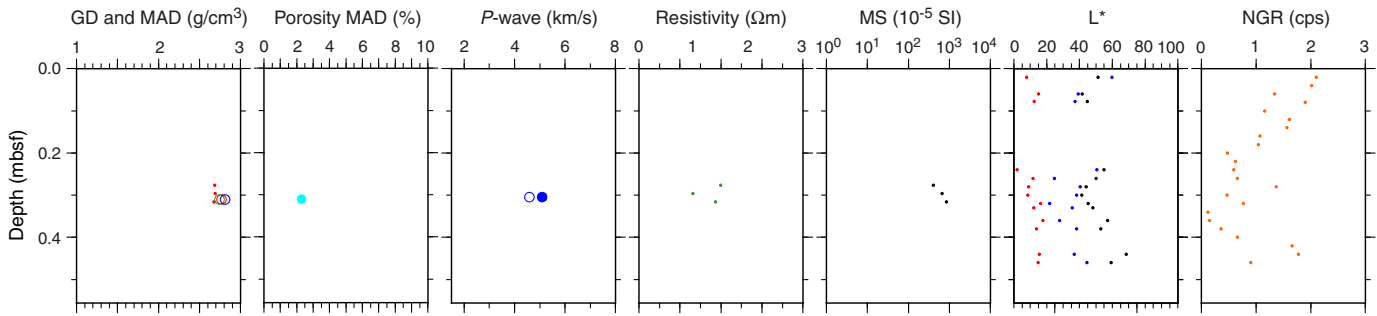
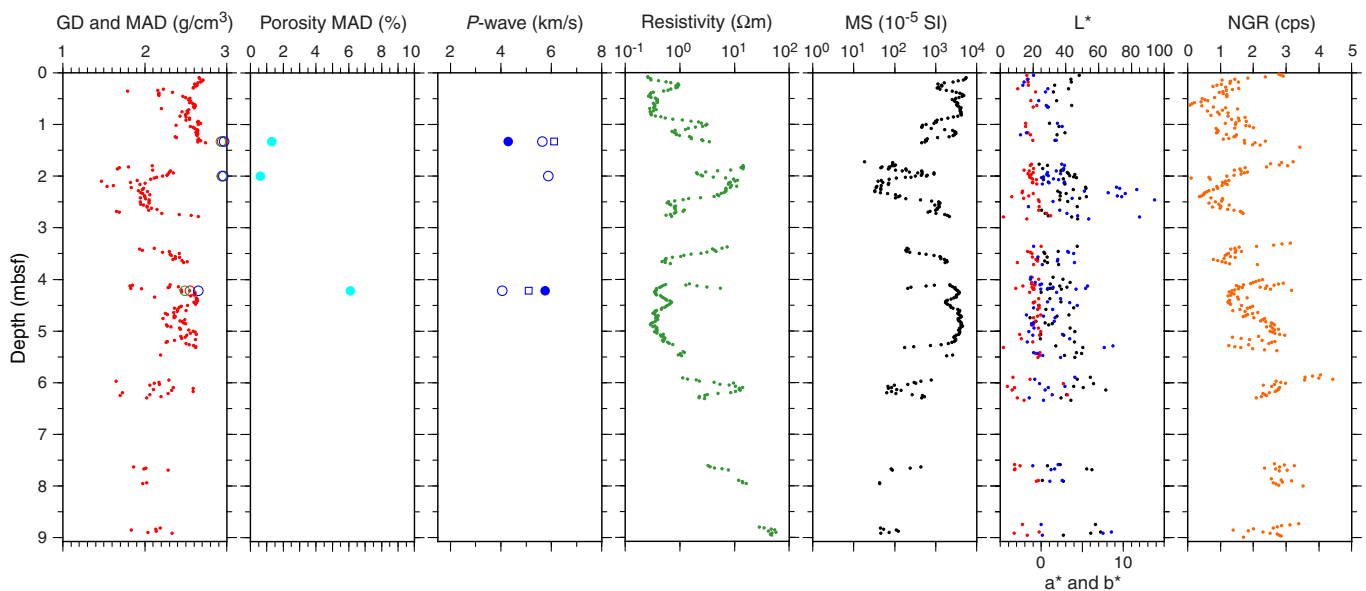


Figure F37. Physical properties from core scanning and discrete samples, Hole M0068B. MAD: red circle = bulk density, green circle = dry density, blue circle = grain density. P -wave velocity: open square = z -direction, open circle = x -direction, blue dot = y -direction. Color reflectance: black = L^* , red = a^* , blue = b^* . Cores 4R and 5R overlap in depth (see [Operations](#)).



The talc-amphibole schist from Hole M0068A is acoustically slower, with a mean of 5.80 km/s (from the two dry measurements taken on the sample; Table T24). The serpentinite sample has the slowest velocity, with an x -direction velocity of 4.05 km/s. The corresponding y - and z -direction velocities (5.75 and 5.10 km/s, respectively) indicate that this sample may exhibit acoustic anisotropy.

Electrical resistivity

Electrical resistivity is very low on average, with a mean of 4.2 Ωm (Table T23; Figures F36, F37). Values range from 0.3 to 57.5 Ωm . Out of all the measurements conducted, 53% are less than 1 Ωm and 89% are less than 10 Ωm . These measurements reflect enhanced fluid contents in the more fragmented core intervals. Local maxima occur at 0.3, 1.0, 1.3, 1.8, 2.1, 2.2, 2.7, 3.4, 4.3, 5.4, 6.1, and 7.7 mbsf. In the lowermost part of Hole M0068B (below Core 8R; 7.8 mbsf), resistivity rises significantly to between 10 and 60 Ωm .

Magnetic susceptibility

Magnetic susceptibility varies between 18×10^{-5} SI and 5522×10^{-5} SI with a mean of 1666×10^{-5} SI and a net decrease with depth (Table T23; Figure F37). Local electrical resistivity minima occur at

the same depths as electrical resistivity maxima, suggesting that the same minerals are responsible for both trends. Considering the recovered lithologies, magnetite, which is produced during serpentinization of ultramafic rocks and may also occur in oxide gabbros, is a likely candidate for explaining these trends. Both the magnetic susceptibility (6.0 SI) and the electrical conductivity (2×10^{-4} to 2×10^4 S/m) of magnetite are high compared to silicate minerals (Telford et al., 1976), so the maxima and minima in electrical resistivity and magnetic susceptibility, respectively, may represent magnetite-poor lithologies in otherwise serpentinite-rich cores. In Core 357-M0068B-4R (4.00–5.72 mbsf), for example, susceptibility and resistivity peaks at 4.3 and 5.4 mbsf, respectively, correspond to gabbroic intrusions in serpentinitized harzburgite and dunite (see [Lithology, alteration, and structure](#)). Apart from these local changes, magnetic susceptibility shows larger scale variations, with the highest values concentrated above 1.2 mbsf and between 3.5 and 5.6 mbsf.

Natural gamma radiation

Site M0068 cores have very low NGR, as expected from the lithologies present (Figures F36, F37). In Hole M0068B, there is a subtle net increase in NGR with depth with maxima at $\approx 0.0, 1.5, 3.3,$

and 5.9 mbsf. The most significant of these (5.9 mbsf; Section 6R-1) corresponds to a unit of subrounded weathered pebbles of variable lithologies (see **Lithology, alteration, and structure**). In situ gamma ray data are also available for Hole M0068B (see **Downhole logging**). The units are in uncalibrated counts per second, and values are therefore not reported here.

Color reflectance

All Site M0068 cores were measured for color reflectance (Figures F36, F37; Table T23). In Hole M0068A, L^* varies between 41.33% and 68.56% with a mean of 50.69%. Mean values of a^* and b^* are -2.60 and 2.61 , respectively. a^* varies between -4.61 and -1.48 , indicating a slightly green color, and b^* ranges between -0.66 and 6.96 . Despite the shallow depth of this hole (0.47 m), highly scattered L^* , a^* , and b^* values are testament to the highly heterogeneous lithologies present.

The L^* of Hole M0068B cores ranges between 18.17% and 64.28% with a mean value of 57.86%. Mean values of a^* and b^* are -1.47 and 2.08 , respectively. a^* varies between -6.86 and 3.17 , and b^* varies between -2.55 and 13.84 . Similar to Hole M0068A, significant scatter in L^* , a^* , and b^* echoes the heterogeneous lithologies, especially between 2 and 3 mbsf. Extremely high b^* values between ≈ 2.1 and 2.5 mbsf in Hole M0068B correspond to an interval of talc-amphibole-chlorite schist (see **Lithology, alteration, and structure**).

Summary

Physical properties from the ≈ 10 m of core recovered across the four eastern holes were acquired during the expedition, including analyses on five discrete samples taken from three of the four holes. Gamma density and NGR are consistent from site to site, and MAD density is systematically higher than density from whole-core measurements. These results were expected, given the variable quality of the core. There is good agreement between the magnetic susceptibility and gamma density data sets. The quality of the core, particularly in rubbly intervals, impacted the gamma density data, creating some scatter in the profiles, but magnetic susceptibility is less affected. A crossplot of density and porosity data (Figure F35) from MAD analyses indicates that gabbro is the most dense and least porous of the lithologies measured, whereas serpentinite is the least dense and most porous. Schists from the eastern area are intermediate in their porosities and densities. Like density, velocity seems to increase from serpentinites to schists to gabbros. Magnetic susceptibility is moderate to high, and the easternmost Site M0075 has lower magnetic susceptibility overall than the more westerly Site M0068. Resistivity is consistently anticorrelated to density and magnetic susceptibility, indicating that porosity is low (supported by MAD analyses), and the electrical properties of the rocks are dominantly controlled by the mineral makeup, rather than porosity. Color data do not systematically vary with any of the other physical properties parameters, which may be in part a function of the discrete (≈ 8 mm spot measurement; see **Physical properties** in the Expedition 357 methods chapter [Früh-Green et al., 2017b]) nature of the measurements (compared to bulk) combined with mineralogical heterogeneity at any given depth. Across the eastern holes, however, a^* values are dominantly negative, indicating green chromaticity, which is unsurprising given the mineralogy of the rocks. Excursions of a^* into the positive, signifying red chromaticity, are relatively rare but tend to coincide with lithologies that have undergone oxidation (see **Lithology, alteration, and structure**). Val-

ues for b^* (negative values indicate blue hues; positive values indicate yellow hues) are far more variable across both sites.

Downhole logging

A 6.1 m long interval of Hole M0068B was logged through-pipe using the OAG tool (see **Downhole logging** in the Expedition 357 methods chapter [Früh-Green et al., 2017b]) over a period of approximately 2 h. A core barrel was stuck in the BHA, preventing deployment of the logging tools in open hole, and therefore in situ measurements were restricted to through-pipe total gamma ray.

Operations

Logging operations commenced at 1020 h on 25 November 2015 following termination of the hole at 9.6 mbsf due to lack of progress. Unfortunately, the core barrel could not be removed from the BHA, preventing the acquisition of open-hole logging measurements. The bit depth for logging operations was reported as 8.3 mbsf, and with the core barrel inside the drill string, the maximum depth the bottom of the tool could reach was ≈ 6.6 mbsf (Figure F38).

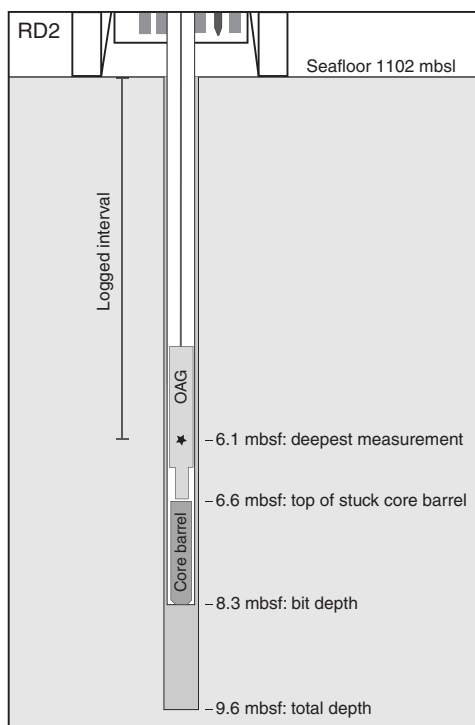
The OAG tool was picked up from its magazine and connected to the wireline cable via the overshot and then initialized. Data acquisition for the winch depth encoder was started, and the tool was then deployed in the drill string, connected to the cable. The maximum depth the gamma ray measurement point reached in Hole M0068B was ≈ 6.14 mbsf. Two full passes of the hole with the OAG tool were undertaken, an initial and a repeat uplog, acquired at a speed of ≈ 180 m/h. Once complete, the overshot was unlatched from the OAG tool, and it was returned to its magazine.

One final attempt to disengage the core barrel from the BHA was unsuccessful, and it was decided to undertake a brief operational test of the deployment of the memory magnetic susceptibility sonde (MSS) (see **Downhole logging** in the Expedition 357 methods chapter [Früh-Green et al., 2017b]), an operation that had previously not been done subsea. Interference of the drill string with the measurement means data from this test are not informative in terms of addressing the scientific objectives of the expedition. The MSS was successfully collected from its magazine, releasing a magnet and triggering initialization of the logging sequence. Similar to through-pipe deployment of the OAG tool, the MSS was connected via overshot to the wireline cable, after which it was lowered through the drill string to the top of the stuck core barrel. Two full passes of the hole were then undertaken before the tool was retrieved to the drill and replaced in its magazine. Logging operations finished at 1213 h.

Data processing and quality assessment

The extremely low levels of natural radioactivity of the formations drilled in Hole M0068B, especially when attenuated through the drill string, make it impossible to identify seafloor on the gamma logs; therefore, the seafloor cannot be used as the reference datum. However, the depth control regarding the location of the seafloor with respect to the RD2 is very good because it is a stable platform sitting on the seafloor and not influenced by the effects of tides, currents, and heave. The depth of the downhole logging measurements is therefore referenced to the amount of wireline cable payed out, the data for which were acquired via a depth encoder during logging operations. The reference log for Hole M0068B was taken as the initial pass from which the repeat pass can be matched

Figure F38. Geometry of logging from the RD2, Hole M0068B.



based on common features in the gamma ray profile. This ensures consistency across the data sets. Undertaking two full passes of the borehole facilitates assessment of the repeatability of the measurement.

Although tool centralization is not essential for the acquisition of good quality NGR data, the intensity of the gamma signal can be affected depending on the position of the logging tool in the borehole. This primarily affects the counts per second rather than the downhole trend. However, because of excellent tool centralization within the drill string, this should not be a factor affecting data quality in Hole M0068B.

The condition of the borehole is normally assessed utilizing a caliper measurement acquired in the open hole. With no such measurement possible in this hole, evaluation of the borehole profile and its potential impact on in situ measurements is not possible.

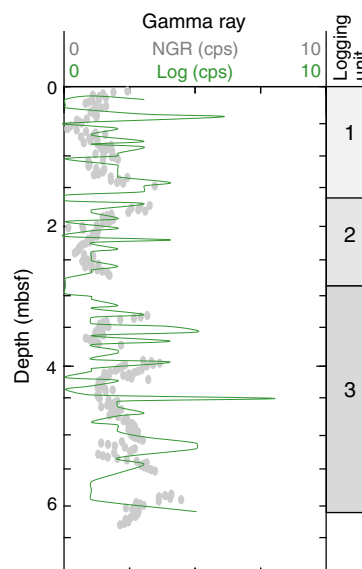
Logging stratigraphy

Three logging units were identified in Hole M0068B on the basis of distinctive features in the gamma ray profile excluding any information arising from the cores recovered from the hole. NGR intensity is consistently low through the logged interval, with a maximum value of 8 counts/s. There is a net increase in gamma ray intensity with depth. Figure F39 includes logging unit boundaries, and a description of the in situ data follows.

Logging Unit 1

Logging Unit 1 (≈ 0 –1.6 mbsf) is characterized by low levels of NGR (mean = 1.8 counts/s), and the profile fluctuates with moderate frequency and relatively high amplitude with depth. The maximum gamma ray intensity is 6 counts/s at 0.45 mbsf.

Figure F39. Total gamma ray downhole logging measurements (green) and core data (gray), Hole M0068B.



Logging Unit 2

Moving downhole into logging Unit 2 (≈ 1.6 –2.9 mbsf), NGR decreases slightly (mean = 1.1 counts/s), and variation, although at a similar frequency, has lower amplitudes compared to the overlying unit. The maximum gamma ray intensity is 4 counts/s at 2.21 mbsf, and there is a subtle net decrease in gamma ray intensity with depth.

Logging Unit 3

The deepest of the logging units, Unit 3 (≈ 2.9 –6.1 mbsf) is distinguished from the overlying units by lower frequency, higher amplitude variations in the profile downhole. Overall, gamma intensity is higher in this unit, with a maximum of 8 counts/s (4.48 mbsf) and a mean value of 2.5 counts/s. There is a subtle net increase in gamma ray intensity with depth in this unit.

Core-log correlations

A complementary NGR data set was acquired from whole-round cores (see [Physical properties](#); see [Physical properties](#) in the Expedition 357 methods chapter [Früh-Green et al., 2017b]) at the Bremen Core Repository (Germany) ahead of the OSP. Similar to the gamma sensor in the OAG tool, these core measurements utilized a scintillation crystal coupled to a photomultiplier tube to ascertain the intensity of the natural radioactivity of the formations encountered. It is therefore reasonable to compare the data sets; however, the heterogeneity of the geology, the core recovery, and the difference in geometry of the measurements mean that it is not expected for correlations to be perfect.

Figure F39 presents the two gamma ray data sets (in situ downhole and whole core) that seem to have some similar features, notably gamma intensity highs at ≈ 1.5 , 1.7, and 4.0 mbsf (depth of downhole measurement). There is clearly a depth offset due to the uncertainty in the original in situ depth of the core material recovered because core recovery was less than 100%.

Paleomagnetism

To achieve the main paleomagnetic objectives, magnetic susceptibility measurements (κ) and rudimentary analyses of natural remanent magnetization (NRM) were made on discrete specimens of known volume and mass (see [Paleomagnetism](#) in the Expedition 357 methods chapter [Früh-Green et al., 2017b]). Four discrete samples were obtained from Site M0068 (Holes M0068A and M0068B), and one discrete sample was obtained from Hole M0075B.

The magnetic susceptibility of the samples taken from Holes M0068A and M0068B ranges between 0.00520 and 0.04470 SI units through the sequences (Table T25).

The NRM direction and intensity of the discrete samples were measured using the 2G-Enterprises SRM 755–4000 magnetometer. Results indicate that an alternating field (AF) of 5 mT is sufficient to remove a weak viscous remanent magnetization (VRM). There were two different responses to this sequential AF demagnetization: Site M0068 samples lost 50% of their NRM intensity at AFs between less than 10 and 20 mT (Figure F40), but the Site M0075 sample showed demagnetization typified by a paleomagnetic vector smoothly demagnetized up to the maximum AF demagnetization level of 100 mT (Figure F41). With a vector that does not trend toward the origin of the orthogonal projection, this magnetic behavior indicates that a characteristic remanent magnetization (ChRM) cannot be isolated for the Site M0075 sample, and it is not possible to determine the inclination value. The paleomagnetic stability of the Site M0068 samples was suitable for AF demagnetization, and it was possible to isolate a ChRM. Inclination data from Holes M0068A and M0068B are negative and very shallow, ranging from -3.2° to -4.4° (Table T25). These results are not compatible with the expected inclination predicted by the geocentric axial dipole model of -49° for this site; however, this incompatibility is consistent with the rubble material drilled at this site. These results preclude the use of paleomagnetic data from the eastern sites for relative dating purposes.

Table T25. Magnetic susceptibility and NRM inclinations of discrete samples, Sites M0068 and M0075. [Download table in .csv format.](#)

Figure F40. Typical AF progressive demagnetization from four samples, Site M0068. Plotted points = successive position in orthogonal projection at the endpoint vector. Solid symbols = projections on vertical plane, open symbols = projections on horizontal plane.

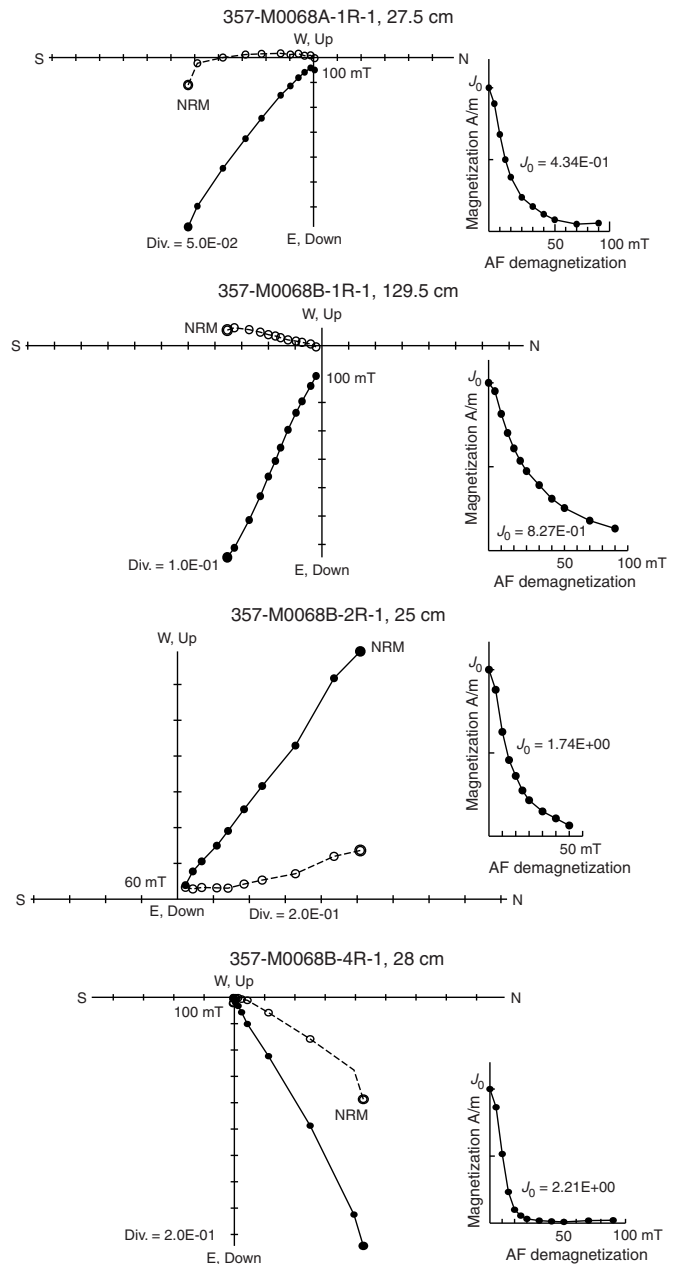
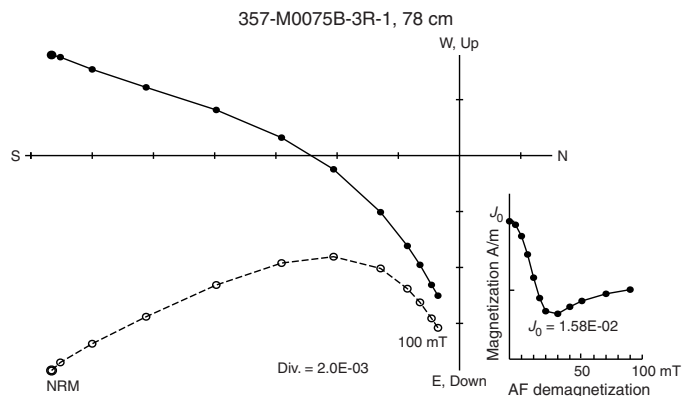


Figure F41. Typical AF progressive demagnetization for one sample, Site M0075. Plotted points = successive position in orthogonal projection at the endpoint vector. Solid symbols = projections on vertical plane, open symbols = projections on horizontal plane.



References

- Blackman, D.K., Karson, J.A., Kelley, D.S., Cann, J.R., Früh-Green, G.L., Gee, J.S., Hurst, S.D., John, B.E., Morgan, J., Nooner, S.L., Ross, D.K., Schroeder, T.J., and Williams, E.A., 2002. Geology of the Atlantis Massif (Mid-Atlantic Ridge, 30°N): implications for the evolution of an ultramafic oceanic core complex. *Marine Geophysical Research*, 23(5–6):443–469. <http://dx.doi.org/10.1023/B:MARI.0000018232.14085.75>
- Früh-Green, G.L., Orcutt, B.N., Green, S.L., Cotterill, C., Morgan, S., Akizawa, N., Bayrakci, G., Behrmann, J.-H., Boschi, C., Brazelton, W.J., Cannat, M., Dunkel, K.G., Escartin, J., Harris, M., Herrero-Bervera, E., Hesse, K., John, B.E., Lang, S.Q., Lilley, M.D., Liu, H.-Q., Mayhew, L.E., McCaig, A.M., Menez, B., Morono, Y., Quéméneur, M., Rouméjon, S., Sandaruwan Ratnayake, A., Schrenk, M.O., Schwarzenbach, E.M., Twing, K.I., Weis, D., Whattam, S.A., Williams, M., and Zhao, R., 2017a. Central sites. In Früh-Green, G.L., Orcutt, B.N., Green, S.L., Cotterill, C., and the Expedition 357 Scientists, *Atlantis Massif Serpentinization and Life*. Proceedings of the International Ocean Discovery Program, 357: College Station, TX (International Ocean Discovery Program). <http://dx.doi.org/10.14379/iodp.proc.357.104.2017>
- Früh-Green, G.L., Orcutt, B.N., Green, S.L., Cotterill, C., Morgan, S., Akizawa, N., Bayrakci, G., Behrmann, J.-H., Boschi, C., Brazelton, W.J., Cannat, M., Dunkel, K.G., Escartin, J., Harris, M., Herrero-Bervera, E., Hesse, K., John, B.E., Lang, S.Q., Lilley, M.D., Liu, H.-Q., Mayhew, L.E., McCaig, A.M., Menez, B., Morono, Y., Quéméneur, M., Rouméjon, S., Sandaruwan Ratnayake, A., Schrenk, M.O., Schwarzenbach, E.M., Twing, K.I., Weis, D., Whattam, S.A., Williams, M., and Zhao, R., 2017b. Expedition 357 methods. In Früh-Green, G.L., Orcutt, B.N., Green, S.L., Cotterill, C., and the Expedition 357 Scientists, *Atlantis Massif Serpentinization and Life*. Proceedings of the International Ocean Discovery Program, 357: College Station, TX (International Ocean Discovery Program). <http://dx.doi.org/10.14379/iodp.proc.357.102.2017>
- Früh-Green, G.L., Orcutt, B.N., Green, S.L., Cotterill, C., Morgan, S., Akizawa, N., Bayrakci, G., Behrmann, J.-H., Boschi, C., Brazelton, W.J., Cannat, M., Dunkel, K.G., Escartin, J., Harris, M., Herrero-Bervera, E., Hesse, K., John, B.E., Lang, S.Q., Lilley, M.D., Liu, H.-Q., Mayhew, L.E., McCaig, A.M., Menez, B., Morono, Y., Quéméneur, M., Rouméjon, S., Sandaruwan Ratnayake, A., Schrenk, M.O., Schwarzenbach, E.M., Twing, K.I., Weis, D., Whattam, S.A., Williams, M., and Zhao, R., 2017c. Expedition 357 summary. In Früh-Green, G.L., Orcutt, B.N., Green, S.L., Cotterill, C., and the Expedition 357 Scientists, *Atlantis Massif Serpentinization and Life*. Proceedings of the International Ocean Discovery Program, 357: College Station, TX (International Ocean Discovery Program). <http://dx.doi.org/10.14379/iodp.proc.357.101.2017>
- Früh-Green, G.L., Orcutt, B.N., Green, S.L., Cotterill, C., Morgan, S., Akizawa, N., Bayrakci, G., Behrmann, J.-H., Boschi, C., Brazelton, W.J., Cannat, M., Dunkel, K.G., Escartin, J., Harris, M., Herrero-Bervera, E., Hesse, K., John, B.E., Lang, S.Q., Lilley, M.D., Liu, H.-Q., Mayhew, L.E., McCaig, A.M., Menez, B., Morono, Y., Quéméneur, M., Rouméjon, S., Sandaruwan Ratnayake, A., Schrenk, M.O., Schwarzenbach, E.M., Twing, K.I., Weis, D., Whattam, S.A., Williams, M., and Zhao, R., 2017d. Western sites. In Früh-Green, G.L., Orcutt, B.N., Green, S.L., Cotterill, C., and the Expedition 357 Scientists, *Atlantis Massif Serpentinization and Life*. Proceedings of the International Ocean Discovery Program, 357: College Station, TX (International Ocean Discovery Program). <http://dx.doi.org/10.14379/iodp.proc.357.105.2017>
- Godard, M., Awaji, S., Hansen, H., Hellebrand, E., Brunelli, D., Johnson, K., Yamasaki, T., Maeda, J., Abratis, M., Christie, D., Kato, Y., Mariet, C., and Rosner, M., 2009. Geochemistry of a long in-situ section of intrusive slow-spread oceanic lithosphere: results from IODP Site U1309 (Atlantis Massif, 30°N Mid-Atlantic-Ridge). *Earth and Planetary Science Letters*, 279(1–2):110–122. <http://dx.doi.org/10.1016/j.epsl.2008.12.034>
- McDonough, W.F., and Sun, S.-S., 1995. The composition of the Earth. *Chemical Geology*, 120(3–4):223–253. [http://dx.doi.org/10.1016/0009-2541\(94\)00140-4](http://dx.doi.org/10.1016/0009-2541(94)00140-4)
- Sun, S.-S., and McDonough, W.F., 1989. Chemical and isotopic systematics of oceanic basalts: implications for mantle composition and processes. In Saunders, A.D., and Norry, M.J. (Eds.), *Magmatism in the Ocean Basins*. Geological Society Special Publication, 42:313–345. <http://dx.doi.org/10.1144/GSL.SP.1989.042.01.19>
- Telford, W.M., Geldart, L.P., Sheritt, R.E., and Keys, D.A., 1976. *Applied Geophysics*: Cambridge, United Kingdom (Cambridge University Press).